Myo-Inositol Supplementation Augments Visual System Maturation in Mice

A thesis submitted by

Seth William Vogel

in partial fulfillment of the requirements for the degree of

PhD

in

Neuroscience

Tufts University

Graduate School of Biomedical Sciences

February 2020

Advisor: Thomas Biederer, PhD

Abstract

Aside from macronutrients, breast milk contains hundreds of micronutrients including vitamins, minerals, and bioactive proteins. Though it is almost universally acknowledged that breast milk is the best source of infant nutrition, the precise contributions of various milk nutrients towards human development is incompletely understood. Myo-inositol is a six-carbon polyol conserved in breast milk across mammals that is thought to play a role in brain development. Using the mouse visual system as a model, I found that postnatal dietary supplementation of myo-inositol increases segregation of eye inputs in the lateral geniculate nucleus of the thalamus. In addition, the number of presynaptic inputs engulfed by thalamic microglia was significantly increased. Microglia morphology was unchanged, suggesting no change in activation state. Instead my data are consistent with inositol supporting the selective elimination of retinal inputs that underlies LGN retinotopic refinement and input segregation.

In the primary visual cortex of adult animals I further found a specific increase in the size of Homer+ excitatory post-synaptic puncta. The size of other synaptic markers was not affected. These changes were accompanied by a significant enhancement of visual acuity in awake and behaving adult animals that had been treated with inositol.

To the best of my knowledge no other dietary factors are known to increase microglial engulfment of retinogeniculate terminals, enhance segregation in the LGN, or enlarge post-synaptic specializations. My data suggest new unexplored roles for inositol as a mediator of synaptic refinement and specialization and point to functional consequences for maternally derived factors in brain development of the newborn.

Dedication

I would like to dedicate this work to my dear dad, Eric Vogel, who instilled in me from my earliest years a love of humankind and a desire to improve the lives of everyone around me. Through countless acts of kindness in your profession as a dentist, you showed me how work can be a framework for service as well as bring personal joy. You always strove to raise the quality of care for your patients by minimizing pain and discomfort and improving outcomes. In this pursuit you were both relentlessly innovative and hardworking.

You also gifted me with an abiding curiosity and appreciation for nature. On hikes and campouts together in the beautiful landscapes of Utah you would point out different varieties of plants, help us spot wildlife, and share all sorts of interesting facts about the diversity of the natural world. On our long drives to Mexico, we would stay up late into the night discussing physics and astronomy. My choice of neuroscience as a major was made after a conversation where you told me about some of the research being done by one of your friends in the neuroscience department. Even though this was not your field, you were always eager to learn new things and would collaborate with others to accomplish what you couldn't do on your own.

Most importantly, I want to thank you for your unstinting love and support through times both good and bad. For being a listening ear, a shoulder to cry on, and a shining example of faith and compassion to be emulated. I miss you greatly and am trying to be more like you each day.

Acknowledgments

Without the help of many generous and selfless individuals, my work would not have been possible. I would like to thank especially my advisor Thomas Biederer for allowing me to join his lab and providing an environment of academic freedom where I could pursue whatever interested me. He has always been available to give advice and suggestions, to help me think critically about my work and to refine experiments. If I have grown as a scientist in the past few years it is largely due to his mentorship and support.

All of my research has been supported by the generous donations of Mead Johnson Nutrition. They have been an excellent industry partner and have always been interested in supporting good science no matter where it leads.

My MD/PhD program director, Jim Schwob, has been a great help to me while navigating some difficult times in my graduate school training including a leave of absence following my father's death, changing labs, and returning to medical school mid cycle.

Michael Stark who hired me for my first research position at BYU and who has been a fantastic mentor for many years. My interest in neurodevelopment would never have come about if it weren't for the time I spent in your lab staring at chick brain vesicles under the microscope.

Most of what I know about neuroscience I learned from Michael Brown, one of the greatest teacher I've ever had and a fantastic neuroscientist who never loses sight of the big picture.

For help troubleshooting experiments, feedback on presentations, and being exemplary graduate students, I must thank Michaela Tolmann and Julia Yelick. You two supported me the most through the hardest stage of this journey.

I would also like to thank my mom, JoLynne Vogel, for her unflagging support, confidence in me, and interest in my work.

Lastly, to Erika, my dear wife, thank you for your patience, love, support, encouragement, and for timely reassurances that things will work out when I am feeling overwhelmed. There is no one else I would rather have keep me company at lab on the weekends and no better friend outside of lab I'd rather do handstands on the beach with. I'm grateful you not only put up with my rambling about work, but offer practical solutions. You are the best and brightest wife anyone could ask for.

Table of Contents

List of Tables

List of Figures

List of Abbreviations Used

AMPA: α-amino-3-hydroxy-5-methyl-4-isoxazolepropionic acid
CCM: Candidate Cell Mask
CDF: Cumulative Distribution Frequencies
CM: Cell Mask
CNS: Central Nervous System
CPD: Cycles Per Degree
CREB: cAMP Response Element Binding protein
CTB: Cholera Toxin Beta
CTRF: Corrected Total Regional Fluorescence
DAG: Diacylglycerol
DHA: Docosahexaenoic Acid
dLGN: Dorsal Lateral Geniculate Nucleus
EM: Electron Microscopy
FITC: Fluorescein Isothiocyanate
FS: Fast Spiking
G6P: Glucose-6-Phosphate
GFP: Green Fluorescent Protein
GLUT4: Glucose Transporter 4
GPI: Glycosylphosphatidylinositol
GSK3: Glycogen Synthase Kinase 3
HMIT: H+/Myo-Inositol Cotransporter
IHC: Immunohistochemistry
IMPase: Myo-Inositol-1-Phosphatase
IP3: Inositol 1,4,5-Triphosphate
IP6: Inositol Hexaphosphate or Phytate
IR: Insulin Receptor
IRS: Insulin Receptor Substrate
KO: Knockout
LCPUFAS: Long-Chain Polyunsaturated Fatty Acids
LDR: Late Dark Rearing
LGN: Lateral Geniculate Nucleus
LPS: Lipopolysaccharide
mEPSC: Mini Excitatory Postsynaptic Currents
mGluR: Metabotropic Glutamate Receptor
MHC I: Major Histone Compatibility Class I
MIP: Maximum Intensity Projection
MIPS: L-Myo-Inositol-1-Phosphate Synthase
MRS: Magnetic Resonance Spectroscopy nAChRs: Nicotinic Acetylcholine Receptor
NARP: Neuronal Activity-Regulated Pentraxin
NMDA: N-Methyl-D-Aspartate
NP: Neural Pentraxin
NP2: Neuronal Activity-Regulated Pentraxin
PBS: Phosphate Buffered Saline

PDK1: Phosphoinositide-Dependent Kinase-1
PFA: Paraformaldehyde
PI3K: Phosphatidylinositol-3-Kinase
PIP2: Phosphatidylinositol 4,5-Bisphosphate
PIP3: Phosphatidylinositol 3,4,5-Bisphosphate
PLC: Phospholipase C
PMT: Photo Multiplier Tube
Pyr: Pyramidal neurons
RATS: Robust Automatic Thresholding Segmentation
RGC: Retinal Geniculate Cell
ROI: Region of Interest
RT: Room Temperature
SC: Superior Colliculus
SEM: Standard Error of the Mean
SGLT6: SMIT2
SMIT: Sodium/Myo-Inositol Cotransporter
SMOS: Sialylated Milk Oligosaccharides
TC: Thalamocortical
TGFβ: Transforming Growth Factor β
TRITC: Tetramethylrhodamine
V1: Primary Visual Cortex
V1b: Binocular Primary Visual Cortex
VEP: Visually Evoked Potentials
VGAT: Vesicular GABA Transporter
VGLUT1: Vesicular Glutamate Transporter 1
VGLUT2: Vesicular Glutamate Transporter 2
WT: Wild Type

1 Introduction

1.1 Motivation

Proper nutrition supports healthy brain development, and deficits in specific micronutrients can have long lasting detrimental effects. However, the exact functions of many dietary factors remain ambiguous. Of particular interest is the question of whether early supplementation with certain nutrients in may improve later cognitive function. These questions are just beginning to be explored. Comparing the effects of breastfeeding and alternative neo-natal diets on brain development is a promising approach to address this question.

The prevalence of the recommended 6-month exclusive breastfeeding [1] in the United States is a meager 17%. Breastfeeding is widely acknowledged to confer multiple health benefits to both the mother and child [2]. Among these, though somewhat controversially, is improved cognitive development and functioning. However, for many women who either cannot or choose not to breastfeed, formula feeding is a viable alternative. While modern formulas have vastly improved since first being introduced in the early 20th century, they still vary substantially from human breast milk, especially in terms of potentially bioactive proteins and small molecules. Humanizing infant formula is one method to close the outcome gap between breast and formula fed children and to advance our understanding of the functions of specific micronutrients. Some components of human milk have already been shown to influence brain development [3].

1.2 Overview of visual system

To explore the effects of specific breast milk components, I chose to use the mouse visual system as a model. The visual system offers many advantages because it has a highly stereotyped developmental trajectory, spans multiple brain regions, is well

suited to study synapse formation and pruning, and provides the opportunity to correlate changes to synapses with functional changes by measuring visual acuity.

Retinal ganglion cells (RGCs) carry visual information via the optic nerve from the retina to the centrally located lateral geniculate nucleus (LGN) of the thalamus as well as to other visual centers [4] involved in processing sub-conscious visual information such as circadian entrapment, saccadic eye movements, and the pupillary light reflex. After crossing the optic chiasm, mixed RGC axon fibers contain contralateral and ipsilateral inputs and together constitute the optic tract, which innervates the LGN. Unlike humans and other primates, the mouse LGN lacks laminar structure, but is still segregated into monocularly dominated regions. Retinal inputs are organized both functionally, into core and shell, and anatomically, with a small patch dominated by ipsilateral inputs surrounded by a much larger region dominated by the contralateral eye. Second order vesicular glutamate transporter 2 (VGLUT2) positive thalamic relay cells in the LGN send axons to the primary visual cortex (V1) by way of the optic radiations.

Thalamocortical (TC) projections form driving inputs onto both pyramidal (Pyr) neurons and fast spiking (FS) PV+ interneurons in layer 4 of primary visual cortex, but to a lesser extent in layers 1, 2/3 and 6 [5, 6]. VIP+ and SST+ interneurons also receive thalamic inputs in layer 4, but they are far weaker [5]. The pre- and post-synaptic properties of TC-Pyr and TC-PV synapses differ. TC-Pyr connections are made up of a few strong and reliable synapses with high release probability [7, 8]. About 1/3 of the excitatory post-synaptic currents in these synapses are mediated by NMDARs with the remainder going through GluA2 containing AMPARs [8]. On the other hand, due to their containing more release sites organized in clusters, TC-FS inputs are stronger than TC-Pyr inputs [9]. TC-FS inputs also have higher release probability, lack NMDARs, and have Ca2+

permeable AMPARs that lack GluA2 [10].

Different classes of interneurons in V1 have distinct wiring patterns. SST+ inhibits all other interneuron types and dendrites of pyramidal cells. PV+ mostly inhibits other PV+ interneurons, or the pyramidal cell soma, but to a lesser extent inhibits VIP+ cells. The third class, VIP+ inhibit SST+ interneurons [11, 12]. TC input therefore both directly excites pyramidal cells and indirectly inhibits them through activation of FS PV+ interneurons that contact the cell soma [12, 13].

Some visual features that were previously thought to arise from cortical processing are in fact at least partially resolved in thalamus. For instance, orientation and direction tuning is found in the thalamocortical boutons and their post-synaptic neurons inherit these properties [6]. Visual acuity develops as receptive fields of cortical thalamorecipient pyramidal cells are refined. Surprisingly, this process, though greatly accelerated by visual experience, can still occur in mice totally deprived of visual experience [14].

1.3 LGN Development and Segregation

1.3.1 Activity Independent Segregation

Though mice are binocular animals, they are starkly less so than humans. About 95% of RGC axons decussate a single time at the optic chiasm and synapse with targets in the contralateral hemisphere. The 5% that remain ipsilateral originate in the ventro-temporal retina [15]. Molecular cues such as EphA receptors and ephrin-A ligands help guide growing axons to the proper location, setting up a course retinotopy in the naso-temporal and dorsal-ventral axes in the LGN that is independent of activity and determining the shape, size, and location of the eye specific territories [16, 17, 18, 19, 20, 21]. These membrane tethered proteins are attached by glycosylphosphatidylinositol (GPI) anchors and expressed in a gradient

across the retina (ephrins) and target regions (EphAs). EphA4/5 repel cells with high levels of ephrin-A2 upon cell contact. It is not clear what process sculpts the dorsal ventral mapping of inputs. In experiments where the optic nerve is redirected to ectopic locations, axons will still segregate according to local EphA gradients [22]. Axons from the contralateral eye reach the LGN first—by E15-16 in mice—with ipsilateral inputs arriving around P0-2 [23]. Molecular gradients define rough territories for axon outgrowth such that by birth there is a crude retinotopic map with thalamic relay cells and cortical cells having broad receptive fields [15]. Ephrin-A2/3/5 triple knockout (KO) animals have profound defects in retinotopy, but it is not entirely random, suggesting that molecular guidance cues act in parallel with other mechanisms to determine the final pattern of connections [24, 25]. There is initially broad overlap between the inputs from the two eyes [15], an arrangement that is resolved with the onset of spontaneous activity and subsequent eye input refinement.

1.3.2 Activity Dependent Segregation

Between birth and P10, refinement of retinal inputs occurs as the territories covered by each axon terminal are pruned and eye specific domains develop [23, 26]. This process occurs in the absence of vision. Even before photoreceptor cells are able to transduce light [23], the RGCs fire in infrequent spatially restricted waves of coordinated local activity that are randomly generated across the retina so as to cover the entire retinal surface over time [27, 28, 29]. These waves are divided into three stages and play an important part in activity dependent input segregation and refinement before the onset of vision [30].

Stage I waves are mediated by gap junctions that link neighboring RGCs and are present from E17 to P1 just after birth [31, 29].

Stage II waves rely on acetylcholine signaling and occur from P1-P10. They drive

the nasal-temporal (visual azimuth) refinement of the retinotopic map in the LGN [32]. The wave period is between one to two minutes and the spatiotemporal origins of the waves are seemingly random and not coordinated between the eyes. This means that there is a very low probability that regions from the two retinas corresponding to the same part of the visual world will generate waves at the same time. During waves there is a high degree of local correlation, a byproduct of gap junctions and starburst amacrine cells that link neighboring RGCs [33, 27]. This local spatiotemporal correlated firing during Stage II waves causes summation of current injections on the target relay cells in the LGN. Without correlated activity, such as in the β2nAChR$^{-/-}$ model [34], individual mini excitatory postsynaptic currents (mEPSC) never depolarize sufficiently to remove the Mg^{2+} block and fire the cell. Spontaneous activity caused by retinal waves leads to calcium influx into thalamic relay cells. One source of calcium is via NMDA receptors, which are more prevalent in the early postnatal period and act as coincidence detectors since a certain amount of depolarization must occur to relieve the Mg2+ block [35]. Coordinated firing of neighboring RGCs combined with a high degree of convergence onto thalamic relay cells allows for spatial and temporal summation of inputs and the opening of NMDA receptors. A second source of calcium is from voltage-gated long lasting (L-type) calcium channels. As the name implies, these channels cause a prolonged calcium influx also called a plateau potential. These channels have an activation threshold of -40 mV. L-type calcium channels open on sufficiently depolarized relay cells. The slow delay kinetics of the NMDA channel contribute to additional temporal summation of EPSPs and decreasing NMDA activity over the first two postnatal weeks is one reason plateau currents become increasingly rare. The calcium influx from L-type calcium channels is actually larger and longer lasting than that mediated by NMDA receptors [26, 36]. Ca^{2+} is an important second messenger and might link coordinated activity and post-synaptic

depolarization with pruning and stabilization of synapses via cAMP response element binding protein (CREB) signaling and changes in transcriptional profiles. Ca^{2+} influx leads to phosphorylation of CREB at three serine residues [37]. CREB signaling is known to be important for synapse survival and specification and is an important downstream regulator of BDNF signaling [38]. These current plateaus occur frequently during development and are seldom seen in adulthood as feedforward inhibitory circuitry matures.

Eye specific segregation and refinement of the retinotopic map are thought to be encoded by stage II waves through a Hebbian mechanism due to their near neighbor correlated firing [39, 40]. At P3, the ipsilateral dominated region covers nearly 60% of the dorsal LGN (dLGN), but this drops to 25% by P7 [15]. The process of gradually segregating into eye-specific zones is largely complete by P10 [41] and by P14 the ipsilateral patch has receded to cover only about 10% of the dLGN, the same as in adult.

How exactly do retinal waves influence the refinement of retinotopic maps? Early on, retinogeniculate axonal arbors are diffuse, leading to broad receptive fields and a high degree of overlap between eye inputs. Most thalamic relay cells receive a plethora of weak excitatory glutamatergic synaptic inputs from both eyes [42, 26], estimated to cover over 50% of the cell surface area at P7-9. At eye opening, the inputs have reduced in number substantially. By P21 only 1-5% of the surface area is associated with presynaptic inputs [15]. Whereas in cats and primates visual information from the two eyes is kept separate until combining in the cortex, rodents do not develop a separate monocular ipsilateral pathway. Instead, binocular responsiveness predominates in the ipsilateral eye territory of the LGN. The size of thalamic relay cell dendritic trees exceeds the average width of the ipsilateral patch and therefore spans both eye specific regions [43]. Innervation from both eyes allows

for activity dependent competition. While either eye could in theory activate a given relay cell, the relative density of inputs from each is not equal. For example, even before activity dependent refinement, relay cells deep in the future contralateral domain receive fewer contacts from the ipsilateral eye, while those in the future ipsilateral patch receive many more. Coordinated firing of neighboring RGCs in the retina strengthens those inputs that successfully depolarize the cell, which will gradually favor the eye with denser inputs.

The function of stage II waves was greatly facilitated by the discovery of several methods to block or manipulate them. They can be specifically blocked by epibatidine [32, 44], an antagonist of nAChRs, or have the coordination of their firing disrupted as in the β2-nAChR-/- mouse. In both cases eye input segregation fails to develop normally [20]. When stage II is blocked in a single eye by injection of epibatidine, the injected eye loses territory in the binocular retinotopic regions of the LGN while the untreated eye expands. This suggests that competition between the two eyes is essential and is controlled at least partially in an activity dependent manner. Much has been written about whether retinal waves are permissive or instructive to input segregation. To some degree the debate may stem from disparate observations in ferret [32] and mice [31]. Rather than requiring a minimum amount of activity, the relative degree of activity between the two eyes is crucial for deciding which eye's territory will expand. Stellwagen and Schatz (2002) observed that increasing the activity levels of one eye was sufficient to cause that eye to gain territory even while the untreated eye maintained physiological levels of spontaneous activity [45].

Stage III waves mark a transition from cholinergic to glutamatergic signaling in the retina and coincide with closed eye vision in mice from about P11-P14 [46]. They are more spatially restricted than stage II waves and are thought to instruct the

refinement of "On-Off" receptive fields [47, 48].

During the third phase of thalamic circuit refinement, roughly from P20-30, patterned visual experience shapes continued refinement of the retinogeniculate synapse. Early experiments using late dark rearing (LDR) showed the necessity of visual experience for the final stage of thalamic maturation [49]. Indeed, recently excitatory corticothalamic projection neurons in layer 6 of V1 have been shown to send instructive feedback signals to the thalamus which influence feedforward circuit refinement. These signals are propagated through numerous weak direct inputs onto thalamic relay cells and via disynaptic routes involving activation of local inhibitory neurons or thalamic reticular nucleus inhibitory interneurons [50, 51]. Cortical feedback inputs convey higher level processed visual information and also signal differently than retinal inputs. For example, retinal inputs signal only through ionotropic NMDA and AMPA receptors, while corticothalamic inputs, in addition to these receptors, also utilize mGluRs [52, 53]. Furthermore, the cortical inputs express a different isoform of vesicular glutamate transporter, VGLUT1 rather than VGLUT2, which affects their pattern of firing. VGLUT1 has faster vesicle recycling but lower release probability [54]. Disruption of corticothalamic projections in layer 6 of visual cortex during the late phase of thalamic development leads to proliferation of weak retinogeniculate inputs [55].

The interplay between cortical and thalamic development is not unidirectional. The binocular responsiveness of relay cells in the ipsilateral patch allows for a possible activity dependent thalamic contribution to ocular dominance (OD) plasticity. Indeed, thalamic contributions to OD plasticity in adult mice have recently been demonstrated. This process involves accentuated responses in the non-deprived eye and requires $\alpha 1$ containing inhibitory synapses [56]. Possibly this increased gain is mediated by the reactivation of functionally silent synapses on binocularly

innervated LGN relay neurons following onset of monocular deprivation [57]. Plasticity of retinogeniculate synapses clearly plays an important role in the maturation of cortical visual processing.

1.4 Regulation of Microglial Synaptic Pruning

Coincident with this phase of refinement the number of active synapses is reduced by microglial phagocytosis [58]. Microglia are the resident macrophages of the brain, they make up 5-12% of cells in the brain and are regionally diverse [59]. Astrocyte-derived transforming growth factor β (TGF-β) causes RGCs to upregulate their expression of C1q at weakly activated synapses [60]. C1q is highly expressed in the LGN during the peak pruning period (P5-10) and localized to synapses. Its expression decreases sharply as segregation wraps up around P14 [58]. C1q is the initiator protein in the classical complement pathway and its expression by neurons leads to deposition of the C3 and C3b complement on nearby synapses. This is thought to act as an opsonin that tags weak imprecise synapses for removal [61, 62]. Recently, the idea that microglia can engulf complete synapses has been challenged by Weinhard et al, who showed that only presynaptic material is engulfed [63].

Microglia are the only cells in the CNS that have a C3 receptor and they are drawn to C3-tagged synapses possibly by neural pentraxin (NP) chemoaffinity [41]. NPs are related to C-reactive proteins and acute-phase proteins. In *in vitro* neuronal cultures, co-culturing with microglia normally decreases the number of synapses formed, however when NPs are knocked out, these synapses are functionally silent, suggesting that NPs might play a role in synaptic maturation. O'Brien et al (1999) showed that neuronal activity-regulated pentraxin (NARP or NP2) are associated with clustering of α-amino-3-hydroxy-5-methyl-4-isoxazolepropionic acid (AMPA) receptors [64]. In the visual thalamus they have been found to co-localize with presynaptic retinal inputs marked by CTB. The strengthening of retained synapses

may in part be due to insertion or clustering of AMPA receptors. In *Np1/2* KO mice, the pruning of the contralateral patch, which initially occupies nearly 100% of the dLGN, fails to occur and the shape of the ipsilateral patch is perturbed [41].

Upon recognizing C3 tagged synapses microglia engulf the presynaptic components as well as sometimes entire synapses. Other immune system proteins have been shown to be important in pruning as well such as major histone compatibility class I (MHC I) [65]. Schafer et al. (2012) confirmed that microglia phagocytose presynaptic material by super resolution microscopy, pHrodo, and immuno electron microscopy (EM) showing that presynaptic boutons marked with either cholera toxin beta (CTB) or VGLUT2 colocalized to CD68+ lysosomes found in the Cx3CR1/EGFP+ microglia cell volumes. Knockout of C3 or its receptor led to overabundance of weak synapses, a failure of eye input segregation, and behavioral anomalies [62]. Others have found that depletion of microglia in organotypic slices with clodronate increases the number of excitatory synapses and that replenishing the microglia population rescued the phenotype. Neuronal microglia co-cultures also have far fewer synapses than neuronal monocultures [66].

Following eye input segregation is a second phase of refinement, characterized by consolidation of synaptic inputs. Early on, the degree of retinal convergence is high, with around two dozen weak inputs onto a single relay cell [49]. These inputs come from many different RGCs, which may share functional properties [67, 68]. However, during this latter phase of refinement, these excitatory glutamatergic inputs are reduced to only a 1-3 [15, 42, 36]. The synaptic strength however increases 50-fold, despite the decrease in numbers. Partially this is attributable to the insertion of AMPA receptors as the AMPA/NMDA current ratio is seen to increase four fold [42, 15]. Hong and Chen showed that the change in convergence is due to clustering of presynaptic boutons rather than additional axonal pruning.

Synaptic remodeling continues after eye opening even though eye-specific territories have been mapped out. The degree of retinal convergence decreases sharply, from around 20 inputs per relay cell at P7 to an average of 10 by P28. A few of these remaining inputs are substantially strengthened following consolidation, while the rest are too weak to drive relay cell firing [69]. Hong and Chen found that during this phase of input consolidation, the axonal arbor was remarkably stable and that rather than retracting axon branches, the presynaptic boutons clustered into a few large rosette structures surrounding SMI-32+ proximal dendrites or relay cell somas. Remarkably, this change in input arrangement is reversible in the late dark rearing model [49], suggesting that visual experience, while perhaps not instructive for the formation of synapses, is certainly important for determining which will be stabilized and mature.

Regarding the subcellular localization of inputs onto thalamic relay cells, the retinal inputs show a unique arrangement called a tripartite synapse, or glomerulus, wherein the axon of the RGC, the spine of a proximal relay cell dendrite, and intrinsic inhibitory interneurons all converge at the same synaptic site [53, 70, 71, 72] In the mature brain, retinogeniculate synapses adopt various conformations. Large presynaptic boutons can be perforated by many dendritic spines from the same relay cell with dozens of active zones or be characterized by just a few external spines with a small number of active zones. Smaller presynaptic boutons can form clustered glomeruli structures either around a dendritic spine or surrounding the shaft, with each small bouton containing a single active zone [73, 74].

Cortical development and LGN development also inform one another [55]. Vesicular glutamate transporter 1 (VGLUT1) positive corticogeniculate feedback projections account for approximately 50% of the inputs to the LGN compared to the 5-10% for VGLUT2+ retinal inputs [73, 75, 76]. This difference in VGLUT isoforms may have

functional significance. Compared to VGLUT1, VGLUT2 depresses more rapidly in response to 10 Hz stimulation, reflecting a higher release probability and slower transmitter recycling [54]. Furthermore, Godwin et al (1996) found that metabotropic glutamate receptors (mGluR) 1 and 5 are both expressed in the LGN [53]. mGluR1 was expressed by the thalamic relay cells and is apposed to corticogeniculate inputs on distal dendrites [53]. Activation of mGluR1 was able to switch the firing state of relay cells from burst to tonic [53]. mGluR5 is expressed by inhibitory interneurons at the tripartite synapses where retinal afferents and inhibitory interneuron contact the proximal dendrites of thalamic relay cells.

In addition to mGluRs, glutamatergic inputs to LGN signal through ionotropic glutamate receptors. Prior to eye opening, NMDA currents predominate, but after eye opening AMPA currents quickly become dominant [42].

1.5 Myo-Inositol

I began this study with the intention of finding breast milk micronutrients that might play a role in brain development. Recently, we published what we believe to be the first example of a dietary factor influencing synaptic size and density [3]. Measuring in layer 4 of adult V1, we found that post-natal DHA supplementation increased the density of post-synaptic Homer 1 by 32 $\pm$ 15 %. Presynaptic VGLUT1 was found to be increased by 22 $\pm$ 6 %. Additionally, DHA increased the size of both pre- and post-synaptic specializations by 26 $\pm$ 3% and 18 $\pm$ 3% respectively. In the current study, I focused on myo-inositol, a second such factor that may additionally influences synaptic maturation, refinement, and maintenance.

Inositol is a polyol made up of a ring of six carbons, each with an attached hydroxyl group. It is found in nine isomers depending on the epimerization of said hydroxyl groups [77, 78]. Myo-inositol is the most common isoform [79], representing 99% of the inositol in humans [80]. For this reason I refer to myo-inositol as simply inositol

in the text, although other isoforms do exist.

Sources of inositol include both endogenous synthesis and dietary intake. Endogenous synthesis primarily takes place as glucose-6-phospate (G6P) is converted to Myo-inositol Phosphate and then free Myo-inositol by the enzymes L-myo-inositol-1-phosphate synthase (MIPS) [81] and myo-inositol-1-phosphatase (IMPase) [82] in the liver and kidney. It is also synthesized in brain [83, 84] and in mammary gland [85, 86]. Adult synthesis of inositol is estimated to be around 4 g/day [87]. Dietary inositol is mostly in the form of phytate (inositol hexaphosphate or IP6) [88] which is found in nuts, milk, beans, fruits, cereals, and meat [80, 89, 90, 91]. For a typical western diet, daily intake is estimated to be about 1 g/day [92].

There are three identified inositol transporters: sodium/myo-inositol cotransporter (SMIT) 1 [80, 93, 94, 95], SMIT2 [80], and H+/myo-inositol cotransporter (HMIT) [80, 96]. SMIT1/2 are expressed in brain and kidney [97, 98]. Intestinal absorption of dietary inositol occurs via the SMIT2 (SGLT6) transporter [80] as does translocation across the blood brain barrier [83, 99]. Inositol is found in plasma [86, 100, 88, 101], breast milk [85, 86] and tissues with high glucose utilization such as brain and heart [80].

1.5.1 Functions of Myo-Inositol

One of the functions of inositol is as an organic osmolyte [84], where it moves into astrocytes when extracellular glutamate concentrations are high to maintain the osmotic gradient. It is also speculated to play a role in brain development. Inositol is involved in neurulation and helps prevent folate-resistant neural tube defects [102]. Proton magnetic resonance spectroscopy (MRS) studies have shown that fetal brain inositol are high during the second and third trimester of pregnancy but decrease with advancing gestational age and drop more rapidly after birth [103, 104, 105]. For example, inositol concentration in the thalamus of term infants is 6.3 $\pm$

1.0 mmol/kg$_{ww}$ [106], but declines to 3.5 mmol/kg$_{ww}$ by adulthood [107]. Inositol is thought to play a role in neuronal plasticity, cell growth, and LTD [108].

IP_6 binds to receptors on neuronal cell bodies [109] and to vesicle adapting proteins such as AP-2 and synaptotagmin [110, 111], suggesting it may have roles in regulating neuronal function and transmitter release. It also binds to L-type calcium channels [112] which are activated by stage 2 retinal waves. Higher inositol levels at birth are correlated with improved language scores on the BSID III [113].

Full term inositol concentration in the thalamus is 6.3 $\pm$ 1.0 mmol/kg$_{ww}$ [106], which declines to 3.5 mmol/kg$_{ww}$ by adulthood [107]. Additionally, inositol is critical to insulin signaling where it provides the building blocks of the inositolproteoglycan (IPG) second messengers phosphatidylinositol 4,5-bisphosphate (PIP2) and phosphatidylinositol 3,4,5-bisphosphate (PIP3) and links insulin binding to its receptor with increased surface expression of the glucose transporter 4 (GLUT4) [114, 115, 116, 117, 118, 119, 120]. Inositol levels can be modulated by dietary factors such as long-chain polyunsaturated fatty acids (LCPUFAS) and sialylated milk oligosaccharides (SMOS) both of which serve to increase inositol concentrations [121, 122]. Inositol biosynthesis is regulated by glycogen synthase kinase 3 (GSK3) [123].

Inositol levels are decreased in the aging brain [124, 125]. In aged individuals, inositol concentrations are correlated with performance on visuomotor coordination tasks [125].

The importance of inositol in supporting proper brain function is underscored by alterations in inositol transporters in schizophrenia [126] and reduced concentrations being observed in the brains of patients with major depressive disorder [127, 128]. In fact, 12 g/day of inositol supplementation was found to be therapeutic for depression through an unknown mechanism [129]. Altered inositol metabolism is

also seen in many neurological and psychiatric diseases including Alzheimers [130, 131, 80], bipolar disorder [132, 133], Parkinsons and amyotrophic lateral sclerosis [80], and major depressive disorder [134, 135, 127]. It is also increased in open angle glaucoma in the primary visual cortex [84].

Recently, several systematic reviews and meta-analyses have demonstrated a role for inositol in treating gestational diabetes mellitus [136, 137, 138, 139]. Treated individuals had increased insulin receptor, insulin receptor substrate 1, and Akt2 [119] and had improved results on the oral glucose tolerance test. Inositol also has protective effects for respiratory distress syndrome [140] and can help treat polycystic ovarian syndrome.

1.5.2 Inositol Increases Visual Acuity in Adult Mice

Our group recently used *in vivo* recordings of VEPs in awake animals to show that postnatal dietary supplementation with the long-chain polyunsaturated fatty acid Docosahexaenoic acid (DHA) can improve visual acuity in the mature mouse cortex [3]. Similar to DHA, the monosaccharide myo-inositol was also identified as synaptogenic in one of our early *in vitro* screens. We therefore wondered if inositol might also have a functional effect on visual processing in the cortex.

We recorded VEPs in response to drifting sinusoidal gradients of black and white bar visual stimuli from P28 and P35 mice treated with daily inositol after birth or littermate controls (Fig. 1.1C). VEPs are a type of local field potentials and represent the firing of groups of neurons following visual stimulation. Their utility in determining visual acuity derives from the fact that the visual system is designed to detect edges and contrasts and responds more strongly to patterned stimuli than to flat field illumination. As the spatial frequency of the black and white bars (e.g. fineness of detail) of the pattern increases towards the visual acuity threshold, the corresponding VEP amplitude drops. At the acuity threshold, the pattern is no

longer discernible and yields the same response as a flat gray. Linear regression of many VEP amplitudes following stimulation with spatial frequencies of 0.15, 0.30, or 0.60 CPD of visual field was used to interpolate visual acuity (Fig. 1.1E-F).

Acuity is measured in CPD, with higher numbers representing better visual acuity. P35 control animals displayed visual acuity of 0.543 ± 0.025 CPD (Fig. 1.1G), in line with that published in the literature [141]. Inositol treated animals had a visual acuity of 0.799 ± 0.077 CPD which was significantly higher ($n = 2/7$, $t = 3.13$, $^*p = 0.017$; two-tailed unpaired t-test). The C/I ratios of 2.08 ± 0.241 for control and 2.21 ± 0.346 for inositol treated (Fig. 1.1D) confirmed placement of the electrode in the binocular visual cortex. Results for P28 animals were similar (data not shown). Together, these results indicate that, similar to DHA, dietary inositol supplementation is capable of increasing visual acuity in mature mice. The current study aimed to better understand how inositol increases acuity.

Note: Data and analyses for Figure 1.1 generated by Malik Abouleish.

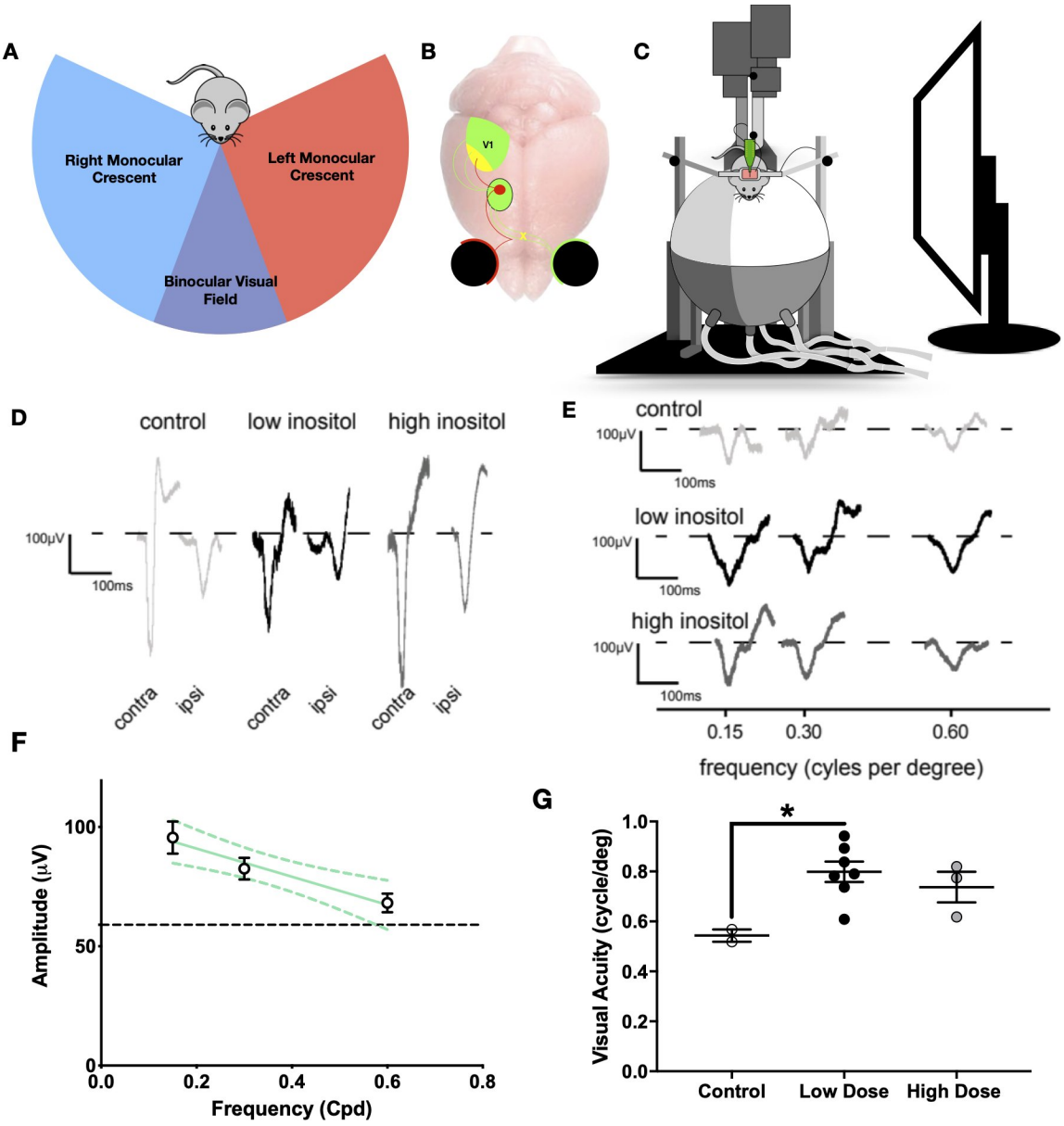

Figure 1.1: Dietary inositol increases visual acuity in mature mouse visual cortex. A) The mouse binocular field. B) Simplified view of the mouse visual system showing retinal ganglion cells synapsing on the lateral geniculate nucleus of the thalamus and the optic radiations connecting thalamus to primary visual centers in cortex. C) VEP recording apparatus for use with awake head restrained animals, which are free to run on a floating Styrofoam ball. D-F) Data from Layer 4 V1b. D) White light response ratio confirm placement in binocular V1. E.) VEPs to high contrast grating stimuli of increasing spatial frequency. F.) Linear regression of P35 low dose inositol VEP amplitudes to calculate visual acuity. Green dashed bars indicate the 95% CI for the regression line, while the dashed black bar represents the mean response amplitude to pre-stimulus noise. G.) Average animal VEP amplitude across treatments. $^*p \leq 0.05$.

2 Materials and Methods

2.1 Mice

All mice used were wild type (WT) C57BL/6J from Jackson Labs (Bar Harbor, ME). Larger litters were culled to have no more than 8 mice. Female breeders were retired after giving birth to and nursing their fifth litter. Animal procedures were approved by the Tufts University Institutional Animal Care and Use Committee and are in compliance with NIH guidelines. Mice were sacrificed by cervical dislocation or an injection of 20 ul/g bw of a 10% ketamine / 1% xylazine mixture in normal saline followed by decapitation.

2.2 Dietary Supplementation

Beginning on postnatal day one (P1), mouse pups were fed once daily with 50 mg/kg body weight myo-inositol (Sigma CAS Number 87-89-8) dissolved in deionized water to a final concentration of 0.1 mg/ul. Littermate controls were fed an equal volume of deionized water. Feeding was done by pipetting the solution into the back of the animal's mouth with a gel loading pipette tip to trigger reflexive swallowing. Measurements of inositol concentration in mouse milk were not available, but at 7 days postpartum, rat milk contains 80 mg inositol / 100 ml [142]. At P10, mouse pups consume an average of 0.95 ml of milk over a 24 hr period [143] which equates to an inositol intake of about 0.75 mg. Myo-inositol was supplemented in the diet at 50 mg/kg bw/day. As the average pup weight at P7 was 3.9 g, the amount of additional inositol was roughly 0.2 mg, an increase of 26%. This estimate is likely to be conservative given that mice probably consume significantly less milk at P7 than at P10. Post-weaning, the mice were separated by sex and fed regular chow (Teklad Global 18% protein, Cat# 2918) ad libitum in addition to continued dietary supplementation or vehicle control. There was no difference in

body mass during the first two post-natal weeks across treatment groups (Fig. 2.1).

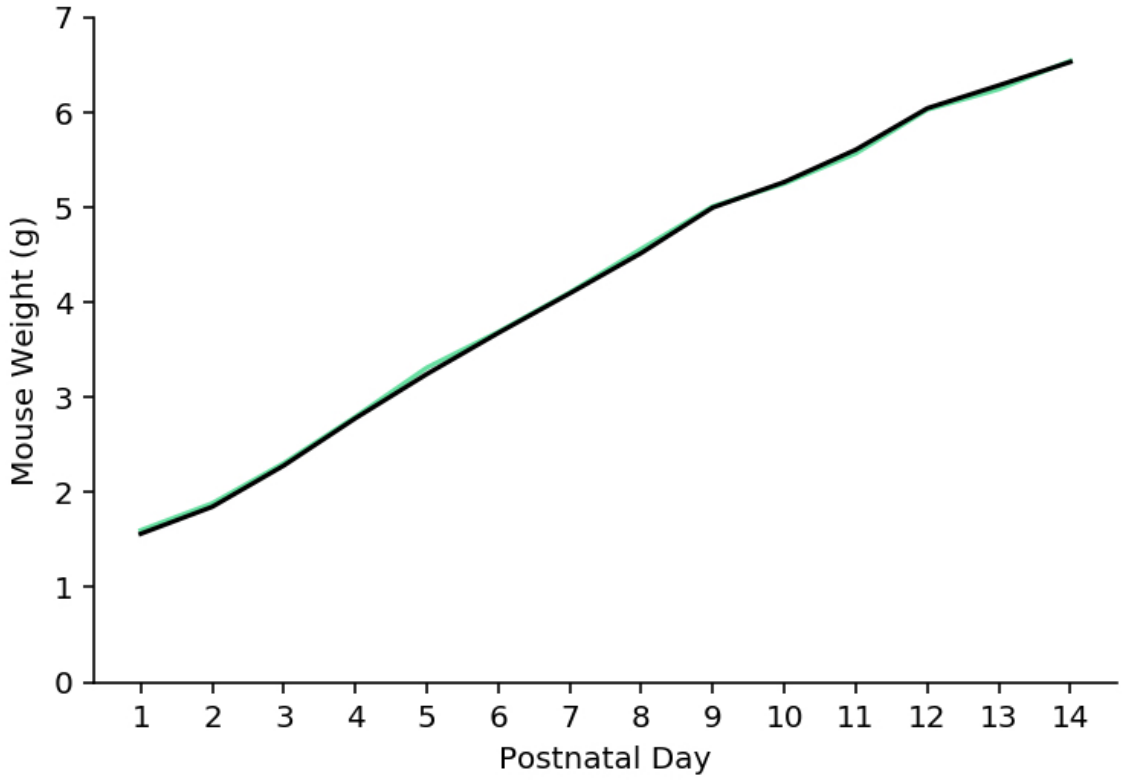

Figure 2.1: Weight Gain Across Treatment Groups Not Significantly Different. Weight of control (black) and inositol (green) treated animals does not vary in the first two post-natal weeks.

2.3 Antibodies

(See Table 2.1 Primary Antibodies)

2.4 Eye Injections

Pups were anesthetized with 7-10 ul per gram body weight of 10% ketamine / 1% xylazine in normal saline given i.p. on postnatal day 5, 8, or 11 and kept on a warming pad (37°C) for a five minute induction period or until a surgical plane of anesthesia was reached. The eyelids were then cut open with a fine pair of scissors and eyes were popped out of the eye sockets with tweezers. 0.75-1.5 ul of CTB [41] conjugated to a fluorescent dye—Alexa 555 for the right eye, or fluorescein

Table 2.1: Primary Antibodies

Target	Manufacturer	Cat. No.	Host	Clonality	Dilution
VGLUT1	Millipore	AB5905	Guinea Pig	Polyclonal	1:1000
VGLUT2		AB2251-I			
IBA1	Wako	# 019-19741	Rabbit		
Homer	Synaptic Systems	# 160 003			1:500
VGAT		# 131 003			1:5000
Gephyrin		# 147 111	Mouse	Monoclonal IgG	1:400

isothiocyanate (FITC) for the left eye—was injected with a Nanoject III injector (Drummond Scientific) into the eye with a fine glass pipette posterior to the limbus and angled toward the back of the retina. Half of the total volume was injected from the dorsal aspect of the eye while the other half was injected ventrally. After injection, the eyes were gently pushed back into the sockets, after which the pups were allowed to recover for 20-30 minutes on a heating pad before being returned to their mother.

2.5 Transcardial Perfusion and Sectioning

For postnatal days 8, 11, or 14, mice which had previously undergone eye injection surgery were transcardially perfused manually using a 27G needle with cold filtered 1x Phosphate Buffered Saline (PBS), pH 7.3, until the liver cleared, approximately 5-10 ml. For adult P35 mice, perfusion was done with a peristaltic perfusion pump (GE Healthcare) with cold filtered 1x PBS, pH 7.3, until the liver cleared—approximately 25 ml—followed by 4% paraformaldehyde (PFA) in 1xPBS, pH 7.3 for approximately another 10 ml. For all mice, brains were then removed and drop fixed for 24 hrs at 4°C in 4% PFA in 1x filtered PBS before being stored in PBS at 4°C, all shielded from light. Fixed brains were sliced in the coronal plane at 75 um thickness on a vibrating microtome (Vibratome 1500, Harvard Apparatus, Holliston, MA).

2.6 LGN Immunohistochemistry

Sections with a large ipsilateral patch in dLGN were identified on a Leica DM5000B upright fluorescent microscope. Slices were blocked for one hour at room temperature (RT) in 1 ml blocking buffer (3% NHS, 0.1% Triton X-100, filtered 1xPBS, pH 7.4). Primary VGLUT2 antibody (Millipore) was made up 1:1000 in antibody dilution buffer (3% normal horse serum, 0.05% Triton X-100, filtered 1xPBS, pH 7.4), 500 ul per well in a 24-well plate with a maximum of three slices in each well. After 48 hrs incubation at 4°C, slices were washed three times for 10 minutes with 1 ml 1xPBS, then moved to 500 ul of goat anti-guinea pig 647 nm secondary antibody (Life Technologies) diluted 1:500 in antibody dilution buffer for 3 hrs. Following secondary antibody incubation, they were washed three additional times. All incubation and wash steps were carried out at room temperature on an orbital shaker and shielded from light unless except where otherwise noted. Finally, sections were floated in deionized water onto glass microscope slides (Fisher), dried, and glass coverslips (Fisher) were mounted with aqua/poly-mount (PolySciences). Slides were cured overnight before imaging.

Single optical sections were imaged with a Leica Sp8 confocal microscope fitted with an HC PL APO CS2 40x/ 1.30 Oil objective (Leica) and a Photo Multiplier Tube (PMT) detector. Laser power, gain, and offset were chosen for each round of immunohistochemistry (IHC) based on the average of manually selected values of several of the control treated slices and then were kept constant while imaging the slides from a given experiment. Each 8-bit 2048x2048 image was acquired at a scanning speed of 400 Hz with 10 frame averages.

2.7 LGN IHC Puncta Quantification

The VGLUT2+ puncta from single optical sections were analyzed in a custom ImageJ macro (code available upon request) that applies a rolling ball subtraction (radius 50 um), a Gaussian filter with $\sigma = 1$, thresholding, and a high pass size exclusion (≥ 0.5 um2) using the built-in ImageJ Analyze Particles tool. The thresholding was carried out with the Robust Automatic Thresholding Segmentation (RATS) plugin of ImageJ. In brief, this approach uses the sum of squares of the Sobel kernel to calculate the input image gradient. Pixels are excluded if the gradient for that pixel is below three times the noise factor, defined as the standard deviation of pixel intensities in a background region. The image is then broken down into small regions with a Quadtree architecture and for each region a local threshold is calculated based on the gradient weighted sum of pixel intensities within the region. Percent area was then measured with ImageJ. A custom built Python program (code available upon request) is then used to determine animal averages of percent VGLUT2 coverage, and run statistics.

2.8 V1b IHC

Antigen retrieval was carried out by placing individual sections in 1 ml of 73°C citrate buffer pH 6.2 for 35 minutes, cooling to room temperature, then washing three times in 1xPBS. Sections were blocked in 1 ml blocking buffer (3% normal horse serum and 0.1% Triton X-100 in 1xPBS) for one hour. Primary antibodies were diluted in antibody dilution buffer (3% normal horse serum and 0.05% Triton X-100 in 1xPBS). Up to three slices were incubated in 250 ul of diluted primary antibody per well of a 24-well plate for 24-72 hrs at 4°C, depending on the antibody (see Table 2.1). This was followed with three ten-minute washes in 1xPBS. Secondary antibody (1:500 in 250 ul antibody dilution buffer) was applied for 2-3 hrs at RT (VGLUT2, VGAT, Gephyrin) or 12 hours at 4°C (VGLUT1, Homer,

NeuN). After secondary antibody incubation, the slices were washed three times as before. All incubation and wash steps were carried out at room temperature on an orbital shaker and shielded from light unless otherwise noted. Slices were then floated onto glass microscope slides (Fisher), dried, and cover-slipped (Fisher) with CFM3 (Citifluor, Hatfield, PA, USA).

Tile scans of the entire binocular V1 (V1b) from a single hemisphere were obtained with a Leica Sp8 confocal microscope with an HC PL APO CS2 63x/ 1.40 Oil objective (Leica) and a HyD detector. Laser power, gain, and offset were chosen for each round of IHC based on the average of manually selected values of several of the control treated slices and were kept constant within a given experiment. Each 12-bit 2048x2048 image was acquired at a scanning speed of 100 Hz.

2.9 V1b IHC Puncta Quantification

10% was cropped off all sides of the images to correct for tile scan overlap and avoid quantifying the same region twice. Background noise levels were obtained for each channel by manually outlining regions of interest (ROIs) for two somas per image that contained minimal staining in that channel. Boundaries between cortical layers were drawn based on the method of [144], for a rectangular selection spanning from the pia to the white matter tracts. The selection was orientated so as to be perpendicular to the white matter. Layer boundaries were then extrapolated from these lines across the merged image following the curvature of the brain surface. All tiles with at least 50% of their area contained within layers II/III, IV, or V were grouped together. For tiles that spanned multiple layers, the layer boundaries were drawn as an image overlay. Single layer ROIs were outlined for each of the selected images using the layer boundaries as a guide where needed, for this experiment layers II and III were treated as a single layer. Robust Automatic Thresholding Segmentation (RATS) was done for each of the channels individually. Puncta size

and number were then quantified with the built-in Analyze Particles tool of ImageJ with no size-based exclusions. A custom Python script (link) was used to average puncta from multiple images and across multiple slices for each animal. Cumulative distribution frequency plots and test statistic distribution plots for the permutation tests were also created in Python (link).

2.10 Corrected Total Regional Fluorescence

Individual tile scan images from V1b were cropped to separate cortical layers when these images spanned multiple layers. The resulting ROI was split into individual channels and the raw integrated density, that is the sum of all pixel intensities within the ROI for a given channel, was measured. To correct for varying background levels, 2-3 small regions of soma were outlined and the average pixel intensity within these regions was used for baseline subtraction. This value was termed Corrected Total Regional Fluorescence (CTRF).

2.11 Eye Input Segregation

The same sections used in LGN IHC were imaged on a Keyence BZ-X710 with a 10x PlanApoλ 0.45 NA objective (Nikon) with the following filter cubes: Green Fluorescent Protein (GFP) (OP-87763) and Tetramethylrhodamine (TRITC) (OP-87764). Exposure was set automatically with slight manual adjustment as needed to reach maximum pixel intensity without saturating more than 2% of pixels within the region of interest. Image format was 1920x1440. Images were acquired in 8-bit.

2.12 Segregation Calculation

Images from the Keyence were sorted by region, converted to 8-bit, and background subtracted (rolling ball, radius 200). Then in a custom Matlab script (code available

upon request), the dLGN was outlined and the pixel intensities of the ipsilateral channel within the dLGN were divided by those of the contralateral channel. The log base 10 of these ratios (termed the R value) was then graphed as a histogram and the variance of all R-values was calculated—hereafter referred to as the segregation index (Fig. 3.1C). Higher segregation indices are associated with decreased overlap between the eye inputs [145]. Values can range from 0 (all pixels have a ratio of 1) to 5.79 (all pixels have intensity of 255/1 or 1/255, split evenly).

2.13 IBA1 Immunohistochemistry

75 um coronal sections from P8 pups were washed three times in 0.3% Triton X-100 filtered PBS for five minutes per wash. They were then blocked for 2 hrs in blocking buffer (0.3% Triton X-100, 1% Bovine Serum Albumin, filtered 1xPBS, pH 7.4). Following blocking, the slices were incubated overnight at 4°C in 500 ul 1:1000 IBA1 primary antibody (Wako). The following day, slices were washed four times for 15-minutes before incubation in the secondary antibody for 2 hrs at RT. After another four 15-minute washes, slices were floated onto microscope slides and dried. Coverslips were mounted with CFM-3 (Citifluor, Hatfield, PA, USA).

2.14 Microglial Engulfment Assay

Method adapted from Schafer et al. (2012) [62]. Z-stacks (step size 0.2 um) of individual IBA1-stained microglia were acquired with a Leica Sp8 confocal microscope equipped with a white light laser, an HC PL APO CS2 63x/ 1.40 Oil objective (Leica) and three Leica HyD detectors. Z-stacks were between 10 and 20 um in thickness. Scanning speed was set to 200 Hz and I used an optical zoom of 2. The image format of 1024x1024 was approximately that of the ideal Nyquist Rate for the shortest wavelength fluorophore. A minimum of five cells were imaged per LGN evenly chosen from all regions.

Rolling ball background subtraction was performed on the two fluorescent channels in ImageJ (radius=20 um) and baseline subtraction was done for the IBA1 channel (baseline=1.5). Three dimensional data was then loaded into Imaris (Bitplane) and a surface object of the microglia was created based on the thresholded IBA1 signal using the default settings and manually adjusting the threshold to capture as many of the fine processes as possible while minimizing the inclusion of noise. This surface object was then used to create a volume mask for the FITC and Alexa 555 channels. Each of the two masked channels was then surface rendered in turn to show the retinothalamic terminals contained within the microglial cell. Thresholding of these channels was done manually to capture puncta. The combined volume of all internalized red and green puncta was reported as a percentage of the total cell volume.

2.15 Microglia Morphological Analysis

For IBA1 morphological analysis, I largely followed the protocol of Kozlowski et al (2012) [146]. An Sp8 confocal equipped with an HC PL APO CS2 20x/0.75 NA IMM objective, two HyD detectors, and a white light laser (all Leica) was used. Two 775 x 775 x 10 um z-stacks (z-step = 1 um) were acquired per animal, each containing one dLGN. Excitation wavelengths were 495 nm (FITC) and 653 nm (Alexa 647). Bandpass filters were 500-622 nm (FITC) and 658-779 nm (Alexa 647). Image format was 1024x1024 pixels, with pixel sizes of $\sim$0.76 um/pixel in X and Y. The Alexa 647 HyD was set to counting mode. Laser powers were 4% and 5% for FITC and Alexa 647 respectively. Images were acquired in 12-bit to provide plenty of dynamic range for heterogeneous fluorescent intensity between images. Acquisition speed was set to 50 Hz so that signal to noise ratio was improved via intrinsic pixel averaging.

Maximum Intensity Projection (MIP) images of dLGN were fed into a custom

written machine learning algorithm in ImageJ for automated segmentation and morphological description. Random coordinates were chosen and a 120 x 120 um rectangular selection was made at each. Within each selection, candidate cell masks (CCM) were generated consisting of connected pixels that were above automatic threshold (Otsu method). Iterative local threshold segmentation then attempted to refine the threshold level until the CCM was within 100 um2 of target cell size (500 um2). After each iteration, the threshold was adjusted by multiplying by the product of the step size (0.01) and a decreasing scaling factor η, which was a cumulative moving average of the difference between target cell size and CCM size for each local region. The iteration loop was terminated when any of four conditions were met. 1.) If no particles greater than 50 um2 were found after automatic thresholding, 2.) the candidate cell area remained unchanged for three iterations in a row, 3.) 100 iterations passed without convergence, or 4.) the CCM area converged to within 100 um2 of target size.

Next, I attempted to correct for any CCMs that touch the local selection boundaries as these might represent only part of the full cell. For these CCMs, I found the center of mass, circularity, and angle of the best fitting ellipse. These were used to calculate a dynamic offset that would reposition the next selection to capture more of the cell by centering it. If the cell continued to abut the selection border after three attempts at repositioning, it was discarded. Similarly, CCMs that had zero or multiple cell somas—defined as a contiguous region $\geq$ 16.7 um2 with pixel values 1.5x the mean intensity of the cell mask—were eliminated. The exact threshold used for detecting the soma is reported to not be important in differentiating activated from resting microglia as the correlation is robust to different thresholding values [146]. Remaining CCMs were considered bona fide cell masks (CMs).

I measured CM area, perimeter, soma size, mean IBA1 intensity, and IBA1

prominence were measured for each detected cell. IBA1 prominence was defined as the mean intensity within the CM divided by the mean intensity of background. Mean background intensity was calculated as integrated density of IBA1 within the whole local region minus the sum of integrated densities for all contiguous groups of pixels in the local region that were both above the current CM threshold and at least 50 um2 all divided by the area of the local region minus the area of the CM.

2.16 Visually Evoked Potentials Recordings

One week prior to recording, mice were anesthetized with 2.0-2.5% inhaled isoflurane for induction and 1.5-1.8% via nose cone for maintenance of surgical plane. After shaving the heads and cutting away about 1 cm2 of skin between the ears, a light aluminum or titanium head mount was fixed directly to the skull using dental cement. Mice were kept on a 39°C heating pad during surgery. After a few days post-operative recovery, mice were acclimated to experimenter handling and to standing on the recording apparatus. Generally this required four 30-minute sessions on the floating Styrofoam ball before the mice were able to hold a set position with minimal postural adjustments. 24 hrs before recording, the mice were again anesthetized as before and a small cranial window approximately 1 mm2 was created with a needle tip over V1b of one hemisphere, located 0.5 mm anterior and 2.0-2.5 mm lateral to lambda (Fig. 1.1B). A separate hole was made over the cerebellum for insertion of a grounding electrode. The surgical site was covered in 3% agarose and a layer of silicone to prevent it from drying out.

On the day of surgery, the animals were head fixed to the recording device atop a floating Styrofoam ball [147] (Fig. 1.1C). A linear 15-um thick 16-channel multi-electrode (model A1x16-5 mm-50-177-A16, Neuronexus, Ann Arbor, MI) was then dropped into V1b to a depth of 450 um [148, 149]. The grounding electrode was subsequently placed in the cerebellum. Brains were kept moist and isotonic by

using small pieces of surgical sponge soaked in normal saline. Once in place, the animal was dark adjusted for 15 minutes while waiting for electrode to settle and the brain to rebound.

2.17 Visual Stimulation

The monitor (AOC) was placed 20 cm from the center of the head and parallel to the plane of the face. The opposite eye was shielded from light with electrical tape placed so as to lay just in front of the eye. Responses to white light stimulation of each eye were measured to determine the contralateral to ipsilateral amplitude ratio. A ratio between 1.4 and 3.3 indicated that the electrode was properly situated in binocular visual cortex (Fig. 1.1D). Visually evoked potentials (VEPs) were then recorded in response to at least 30 minutes of high contrast, sinusoidal drifting gratings with random orientations and spatial frequencies ranging from 0.0-2.5 Cycles Per Degree (CPD). Each stimulus was presented for 1.5 seconds with 0.2 seconds of neutral grey in between. This protocol was adapted from that of Porciatti et al. and Niell et al. [150, 141].

2.18 VEP Analysis

Analysis of VEPs was done in Spike2 v. 8.00 (Cambridge Electronic Design). Artifacts due to mouse movement were identified and deleted manually. Remaining data was binned by spatial frequency and orientation and then averaged within bins. Recordings were of sufficient length to have 5-25 VEPs per bin. VEP amplitude was then measured from the average waveforms, defined as the voltage difference between P0 and N1 [151]. Background levels were calculated as max voltage - min voltage during the 0.2 seconds of gray screen preceding each stimulus. Linear regression of the amplitudes from 0.15, 0.3, and 0.6 CPD was performed and visual acuity defined as the spatial frequency at which this line intercepted the noise

amplitude.

2.19 Data and Statistics

Data is generally presented as mean ± SEM except where noted. All quantifications were performed blind to treatment allocation. Statistical analysis was done with GraphPad Prism software version 8.2.1. For comparison of means between two groups, unpaired two-tailed t-tests were used unless otherwise noted. One-way ANOVA was used to compare multiple groups simultaneously. Cumulative distribution frequency plots were analyzed with an exact permutation test. Briefly, the two-sample Kolmogorov-Smirnov test statistic was calculated with the actual treatment assignments of the animals and then for every permutation of treatment assignment with the same group sizes. The p-value is equivalent to the fraction of all generated test statistics that are greater than or equal to the observed test statistic. Linear regression analysis was used for visually evoked potentials. Normality was checked with the Shapiro Wilk test. P-values less than 0.05 were considered significant.

Mixed models contain both fixed and random effects. My model had one fixed effect (treatment) and one random effect (animal/treatment combination) with random intercepts. For deriving the p-value, a REstricted Maximum Likelihood (REML) ANOVA was performed.

Note: VEP recordings and analysis performed by Malik Abouleish, all other experiments and analyses were carried out by the author.

3 Results

3.1 Increased Eye Input Segregation in P14 dLGN.

The visual system is primarily comprised of the retina, visual thalamus, and visual cortex. An alteration to any of these sub-systems could account for the increased acuity effect. I decided to first look in the visual thalamus because the critical period for its maturation is between P3 and P14 [15, 26], which made this system experimentally the most tractable. During this period the initially overlapping retinogeniculate inputs from the left and right eye compete for territory and segregate into distinct domains [152, 42, 21, 49]. This process is driven by spontaneous coordinated retinal waves rather than patterned visual activity as the eyes have not yet opened [32, 30, 18] and is executed by microglial pruning of synapses [153, 58, 62]. I set out to test whether inositol affected pruning and input segregation during early postnatal life.

On day P8 or P11, mice were anesthetized, the eyelids cut open, and 1-3 ul of CTB conjugated to Alexa 555 (right eye) or FITC (left eye) injected into the dorsal and ventral aspect of the eye behind the lens. CTB anterogradely labels RGCs for visualization of retinofugal projections [152, 58], in mice the primary targets of RGCs are the LGN of the thalamus and the superior colliculus (SC) in the midbrain. ∼95% of fibers from the retina decussate at the optic chiasm, while a small minority remain ipsilateral [21, 26]. After allowing three days for sufficient transport of the dye to these target structures, the mice were transcardially perfused and the brains removed and drop fixed in 4% PFA overnight before being sectioned for imaging (Fig. 3.1A). Dye-conjugated CTB allows the structure of the LGN to be easily discerned and clearly differentiates ipsilateral and contralateral eye inputs (Fig 3.1B).

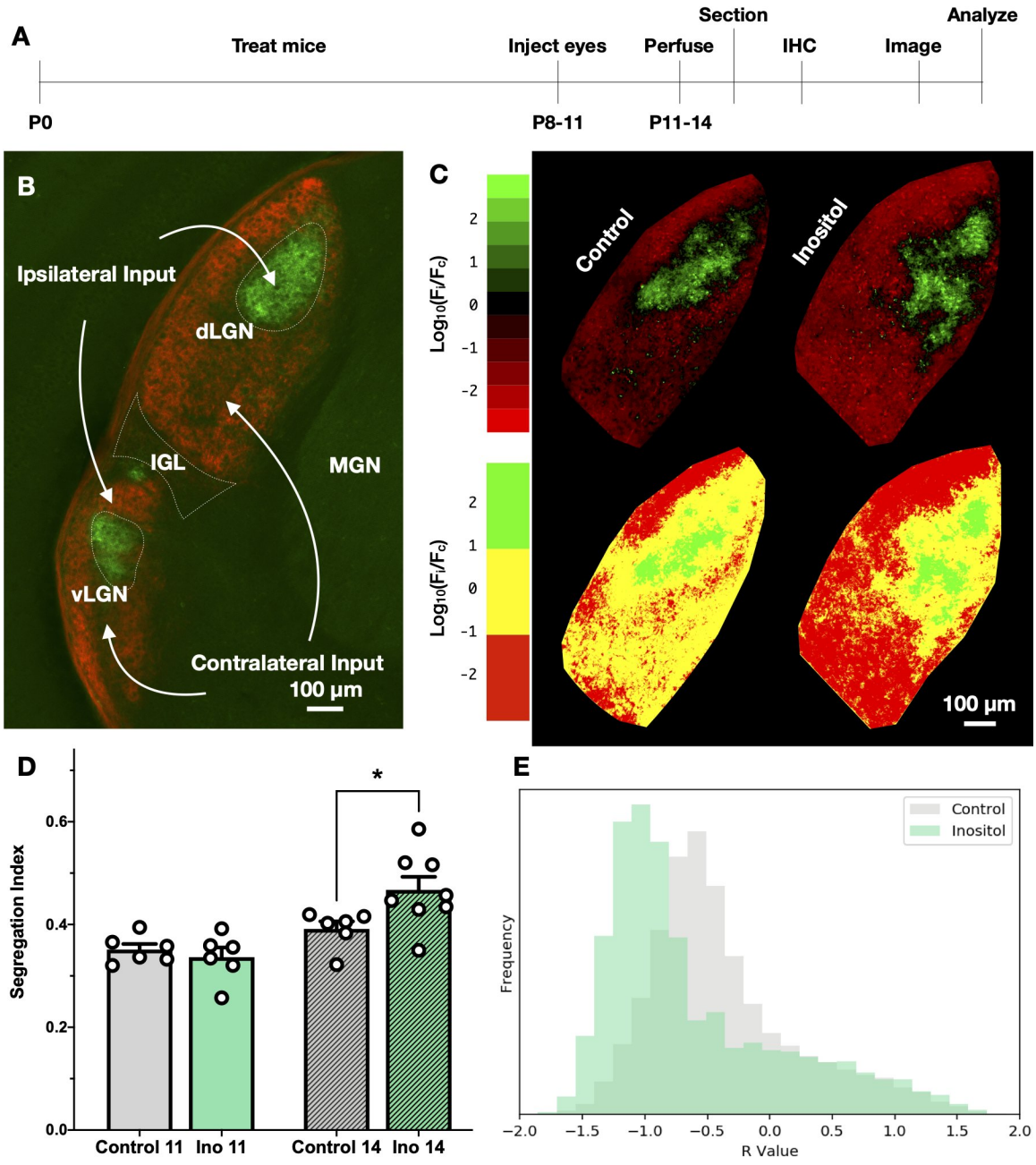

Figure 3.1: Increased segregation of eye inputs in dLGN in inositol treated animals. A.) Starting at birth, C57/BL6J mouse diets are supplemented with 50/mg/kg/day inositol, with vegetable oil as a vehicle control. B.) Low power image showing the sub-nuclei and eye input territories in the left LGN at P14. C.) Representative P14 pseudo-colored R-value maps indicating ratio of eye input strength. More extreme values indicate stronger inputs from one eye versus the other. Bottom: simplified three-color LUT for illustration purposes. D.) Segregation index (variance of R-value histograms) for P11 (solid bars) and P14 (hashed bars) inositol animals versus vehicle control, data from dLGN. (Means compared with unpaired two-tailed t-test, * $p < 0.05$). E.) Histograms showing distribution of R-values from panel C.

For this experiment, I looked at two timepoints. The earlier P11 time point coincides with the onset of closed eye vision, and the end of the normal window for input segregation which is just prior to natural eye opening. The latter P14 time point is post-eye opening and after the segregation of eye inputs is normally complete.

I followed the method of Torborg et al [145] to quantify segregation. Briefly, each eye is injected with a different dye and the degree to which each pixel in the LGN is biased towards one eye over the other is expressed as the log10 ratio of the channel intensities (R value). The segregation of inputs is equal to the variance of the R values with higher values indicating more segregation. Torborg et al. (2004) report an average segregation index of 0.6 for WT P8 animals [145].

At P11 I observed no difference in the degree of input segregation between the control (0.351 ± 0.011) and inositol (0.337 ± 0.019) treated animals ($n = 6/6$, $t = 0.676$, ns) (Fig. 3.1D). However, at P14 I observed a substantial increase in input segregation from 0.391 ± 0.015 for control to 0.468 ± 0.025 for inositol treated; the increase was statistically significant (n=6/8, $^*p = 0.036$, $t = 2.36$; two-tailed unpaired t-test) (Fig. 3.1D). The increase in segregation seems to be primarily driven by enhanced consolidation of the ipsilateral patch. Mixed input pixels are noticeably less prominent in the contralateral dominated region of inositol treated animals while the number of strongly contralateral dominated pixels is increased in the same region (Fig. 3.1C). This is also apparent by comparing the histograms of R values which have a left shifted contralateral peak in inositol treated animals (Fig. 3.1E). Overall, these data suggest that dietary inositol supplementation increases the final extent of eye input segregation in the dorsal LGN of mature mice.

3.2 VGLUT2 Density in dLGN Is Unchanged.

To determine if segregation was being driven by a reduction in retinal inputs, I first turned to immunohistochemistry to visualize the retinogeniculate terminals. Presynaptic boutons from retinogeniculate afferents can be differentiated from the more numerous corticothalamic inputs because the former are VGLUT2+ while the latter are VGLUT1+ [154, 155].

Owing to the fact that VGLUT2 puncta in the thalamus cluster together (Fig. 3.2B) [73, 7], it is difficult to confidently differentiate individual puncta (Dorothy Schafer, personal communication, 7 February 2019). Therefore, instead of looking at puncta size or density, I measured the percentage of each automatically thresholded ROI that was VGLUT2+ following the method of Werneburg et al [156] (Fig. 3.2C). When doing any sort of puncta analysis, the thresholding method is particularly important. Manual thresholding introduces user bias and variability as background intensity levels must be subjectively determined for each image and can vary from user to user or even from day to day. Furthermore, because immunostaining of tissue sections can be uneven the signal to noise ratio varies across the sample and even within different parts of the same image. I addressed these issues by using the built in ImageJ plugin Robust Automatic Thresholding and Segmentation (RATS) to do automated regionally variable thresholding. Using the same two timepoints as before, I examined the coverage fraction of VGLUT2 staining in both the ipsilateral patch and in a second region dominated by contralateral inputs (Fig. 3.2A). I also attempted to measure post-synaptic side changes by staining for the post-synaptic excitatory marker Homer, but technical issues with the staining quality prevented reliable quantification. I observed no significant difference in VGLUT2 coverage between any of the groups (Fig. 3.2D) ($n_{\mathrm{P11}} = 6/6$, $n_{\mathrm{P14}} = 8/9$, $\mathrm{F}_{7,50} = 1.80$, $p = 0.108$; one-way ANOVA).

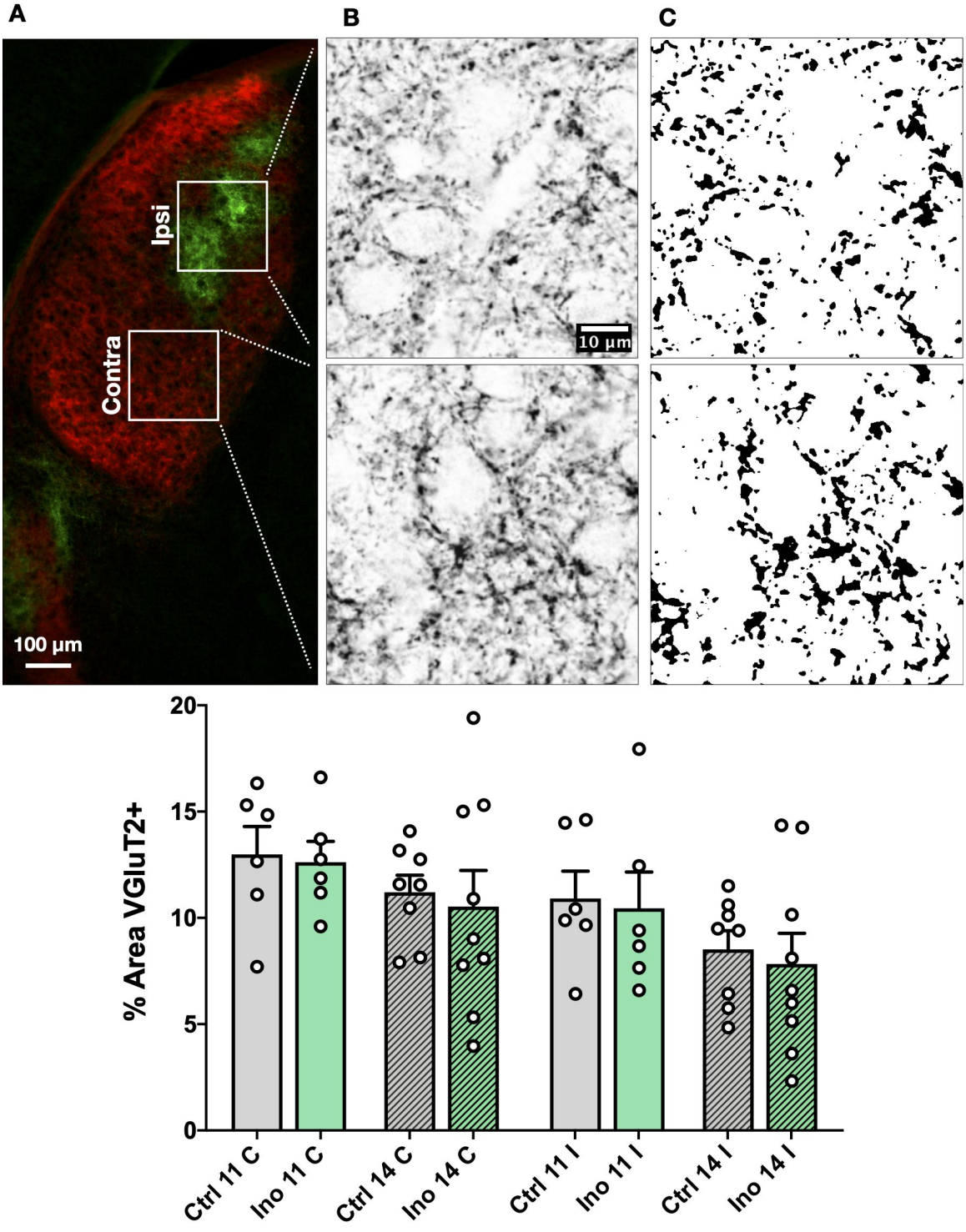

Figure 3.2: Inositol has no effect on VGLUT2 density in juvenile mouse dLGN. A) Low power micrograph of LGN showing regions of interest. B) Representative high power VGLUT2 IHC images from ipsilateral (top) and contralateral (bottom) dominated regions. C) Associated puncta masks used for quantification. D) % fraction of ROI that is VGLUT2+ in the contralateral (C) and ipsilateral (I) dLGN at P11 and P14.

3.3 Microglia Engulfment of Presynaptic Boutons Increased at P8.

The lack of an effect on total VGLUT2 despite increased segregation could be due to the concomitant enlargement of spared synapses, the proliferation of new non-overlapping synapses, or perhaps because the number of synapses needed to be removed to increase segregation is small relative to the whole population. I reasoned that by looking at engulfed material in the microglia themselves, I might increase the sensitivity to detect differences in engulfment that would otherwise be lost amidst the background of non-removed synapses.

I therefore labeled microglia with an antibody against ionized calcium binding protein 1 (IBA1), a 17-kDa actin-binding protein constitutively expressed by the microglia/macrophage population. Using confocal microscopy and Imaris (Bitplane) I made 3D reconstructions of microglia and quantified the fraction of engulfed dye-conjugated CTB within the IBA1+ cell masks (Fig. 3.3B-C). As dye-conjugated CTB has been shown to have excellent correlation with VGLUT2 [73], I deemed staining for VGLUT2 to be unnecessary.

Presynaptic boutons overlapped with the 3-dimensional cell mask and the raw IBA1 signal in both single optical sections (Fig. 3.3A, Fig. 3.4A) and in orthogonal views (Fig. 3.4B). Schafer et al [62], have employed the same approach and cross-validated its accuracy using electron microscopy. Microglia from inositol treated P8 mice contained 28% more presynaptic material, on average occupying 4.33 ± 0.416 % of the cell volume compared to 3.38 ± 0.235 % for control animals (Fig. 3.3D). This difference was significant ($n = 5/6$, $t = 1.88$, $^*p = 0.046$, $df = 9$; one-tailed unpaired t-test). I used a one-tailed t-test for this comparison because I had hypothesized *a priori* that the increase in segregation of eye inputs would be driven by microglial elimination of inputs destined for removal.

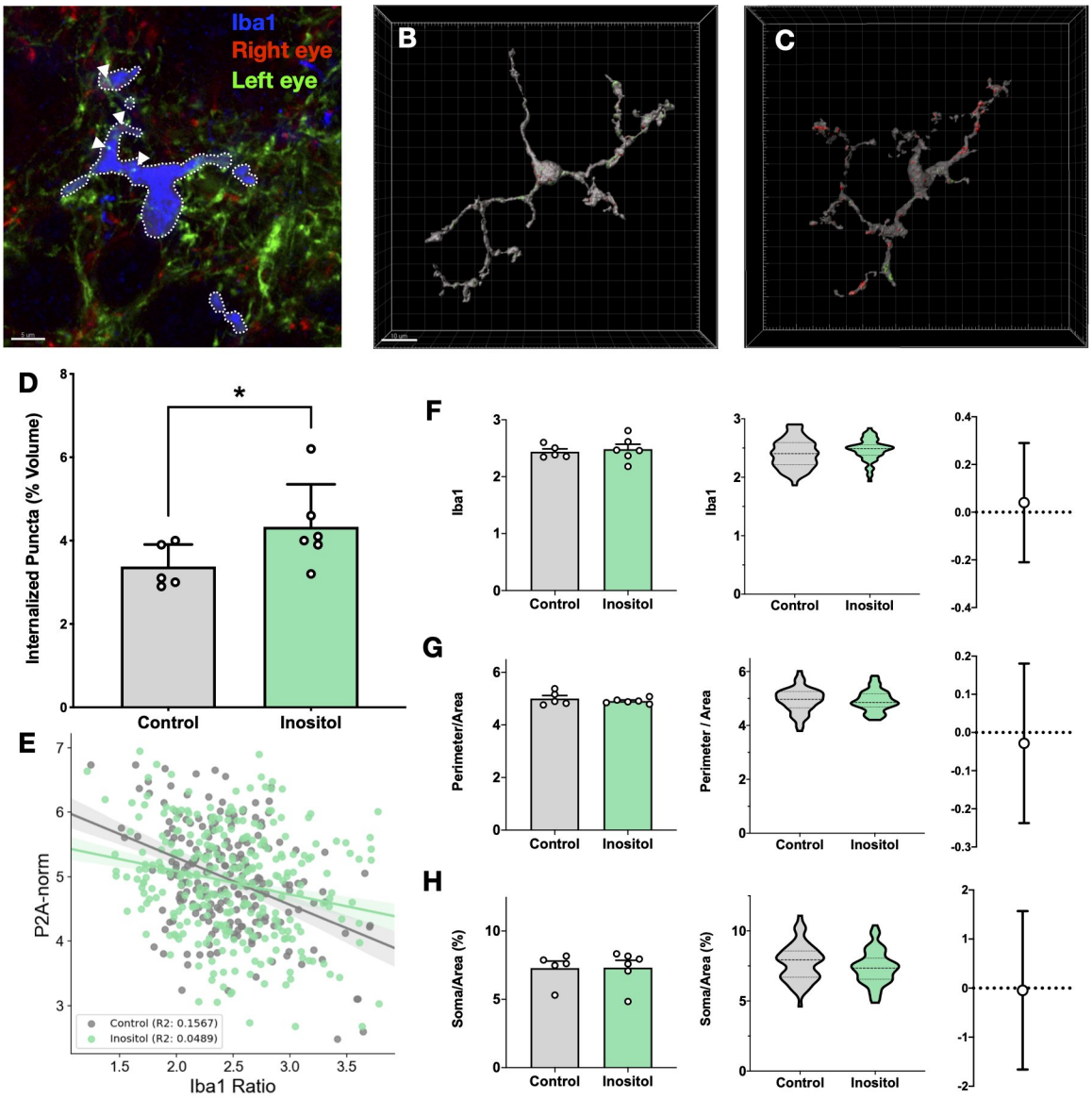

Figure 3.3: Microglial engulfment of dLGN presynaptic retinothalamic boutons increased with inositol treatment. A) Single optical section showing left eye (green) and right eye (red) inputs and IBA1+ positive microglia (blue). Translucent blue overlay represents the cross section of the 3D reconstructed IBA1 channel. B-C) Representative microglia reconstructions with internalized puncta in red and green for control (B) or inositol (C). D) Engulfment index in control (3.38 ± 0.235%) and inositol (4.33 ± 0.416%) treated animals. Means compared with one-sided Student's t-test, $p = .046$. E) Correlation between IBA1 ratio and normalized perimeter-to-area ratio from morphological analysis. Shaded regions represent standard error of slope (bootstrap with blocking at the animal level). F-H) IBA1 ratio, normalized perimeter/area ratio, and soma/area ratio (left) animal averages, (center) violin plots of individual data points, and 95% CI for difference between means (right). Means compared with unpaired two-tailed t-test (left) or nested t-test (right). All differences n.s.

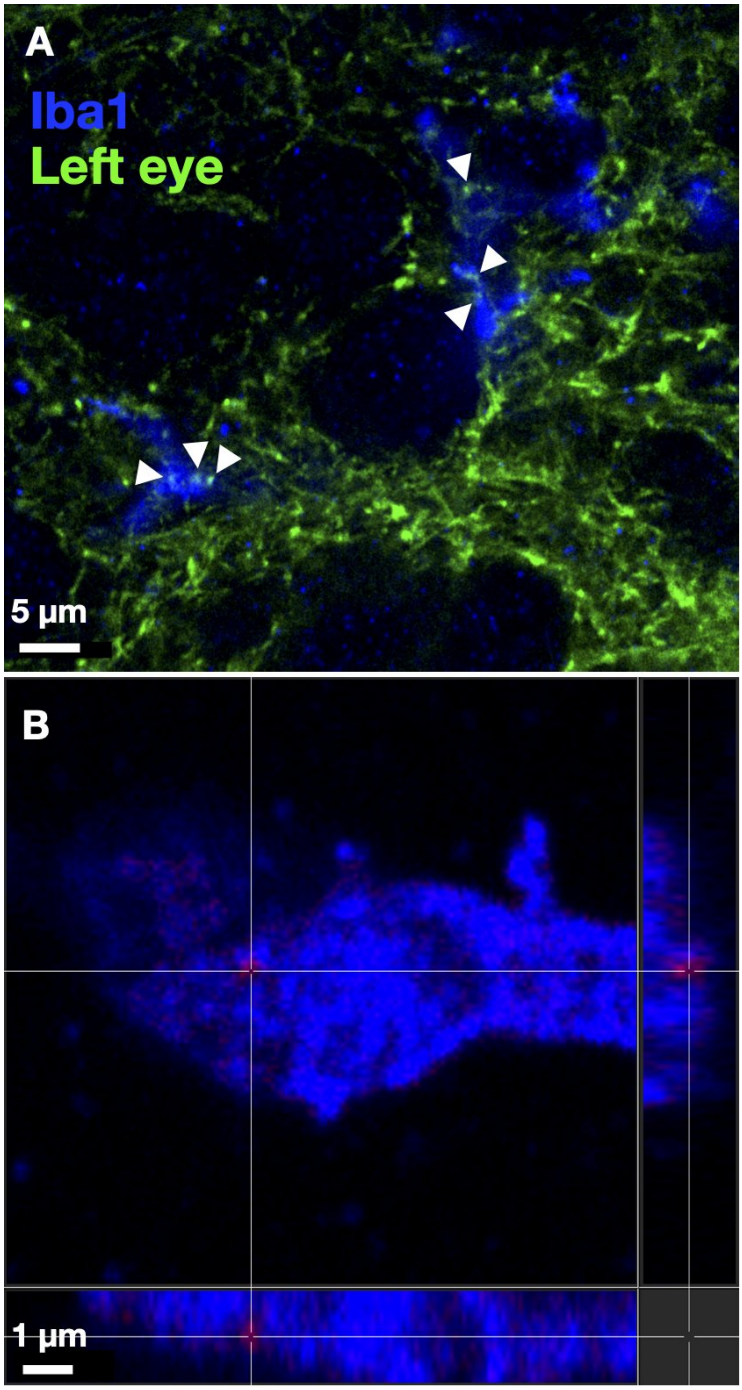

Figure 3.4: Presynaptic material contained within IBA1+ cells. A.) Single optical section of P8 mouse dLGN showing dye-labeled retinal inputs from left eye (green) and an IBA1+ microglia (blue). Internalized puncta shown with white arrow heads. B.) Orthogonal views of a single internalized puncta.

3.4 Microglial Morphology Is Unchanged at P8.

If microglia from inositol treated animals contain more presynaptic material, does this mean that inositol regulates microglial activation? Microglial can adopt many different functional states [157] some of which are defined by increased motility and phagocytosis. In their most common state, microglia are constantly surveying the local environment by extending and retracting their fine processes and interacting with neurons and other glial cell types [158, 159, 160, 161]. In response to injury, infection, or inflammation, microglia switch to other states, with distinct morphological features [162]. Recently, it has become clear that microglia play a crucial role in normal central nervous system (CNS) development and that some of the so-called reactive states may in fact be utilized in physiological contexts as well. For example, active remodeling of synaptic circuitry by microglia is known to occur in the LGN where microglia engulf synaptic material tagged for removal with C1q and C3 [58].

To evaluate changes in microglial morphology, I imaged cells from the same P8 LGN sections used in the engulfment assay. I wrote an automated machine learning based cell segmentation algorithm in ImageJ based on that of [146]. In 10 minutes, it was able to detect 563 cells from 23 low-power images taken from 11 animals. The program requires no input from the user and manual quality control checks found that less than 5% of cells had low quality outlines. Outlines of twenty representative cells are shown in Fig. 3.5. For each cell, I measured several morphological metrics reported to be reliable markers of microglial activation and compared these between treatments.

First I looked at soma size. Soma area is predicted to be increased in more activated microglia as the cell adopts a more amoeboid morphology and the ramified processes retract. In fact, of four morphological measures looked at by Kozlowski et al., soma

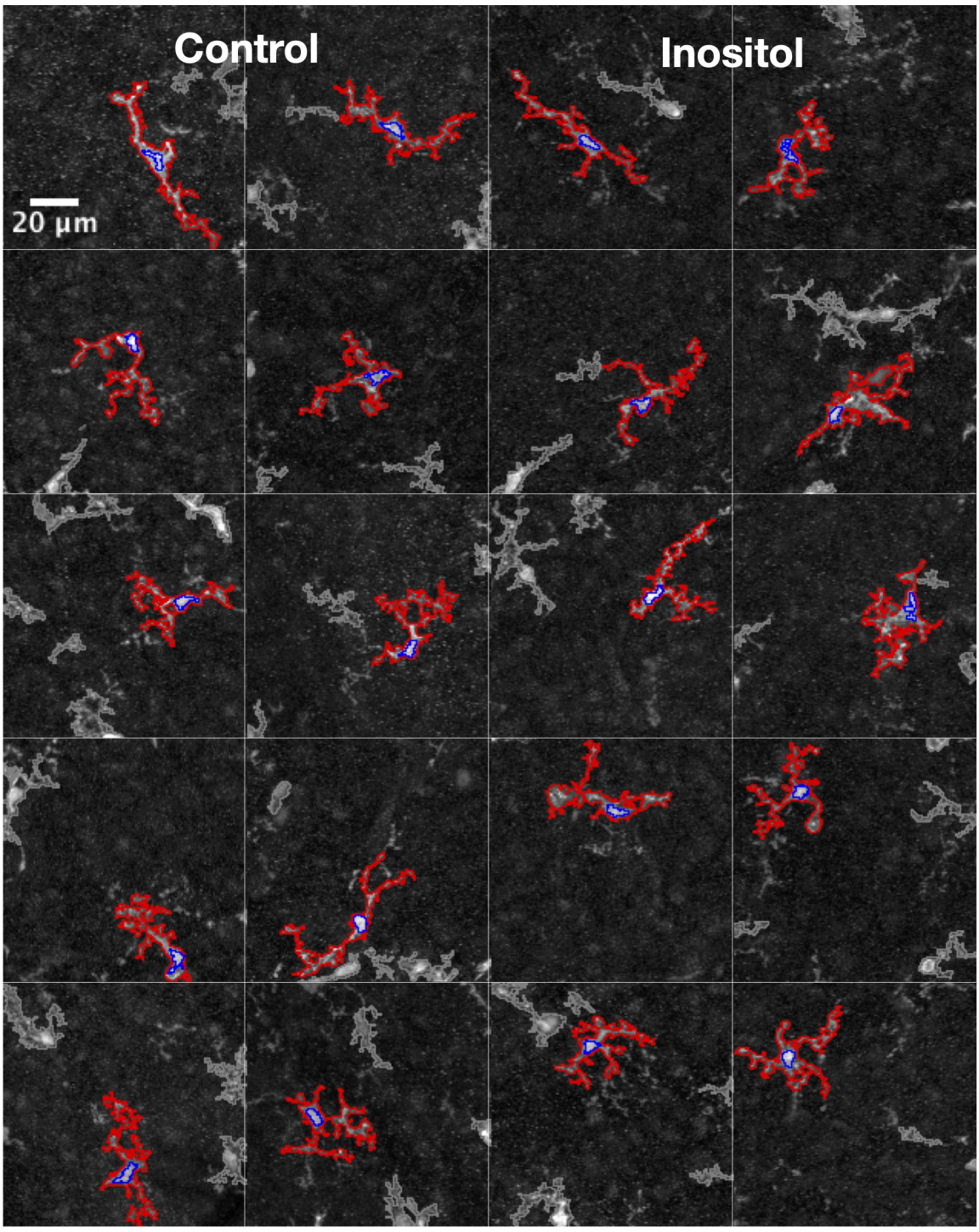

Figure 3.5: Twenty representative automatically outlined microglia from mouse P8 LGN. Somas outlined in blue. Soma minimum size filter was 16.7 um2 and intensity threshold was 1.5x the mean IBA1 intensity of the cell mask. Microglia cell body outlined in red. Target cell size 500 um2, tolerance ± 100 um2. Local IBA1 signal not within cell mask outlined in gray. These pixels were excluded when calculating the mean background fluorescence for determining the IBA1 ratio.

size was found to have the strongest correlation with IBA1 intensity, a relationship that was substantially stronger following lipopolysaccharide (LPS) injection [146].

In my experiment soma area was not affected by inositol treatment (data not shown). The average for control (33.45 um^2) and inositol (34.00 um^2) treated animals was unchanged ($F_{1,9} = 0.031$, ns). These soma areas are, however, consistent with what has been reported in the literature for naïve murine microglia [146].

I next looked at the expression levels of IBA1. Phagocytosis is an ATP-dependent energy intensive process that requires abundant remodeling of the actin cytoskeleton. The constitutively expressed macrophage/microglia protein IBA1 facilitates actin cross-linking and is found in membrane ruffles and phagocytic cups [146, 163, 164]. Its expression is upregulated with microglial activation. To correct for non-homogenous staining intensity in my IBA1 IHC, I report the background corrected intensity of IBA1—the IBA1 ratio—rather than an absolute intensity. Cells adopting a phagocytic profile would express higher levels of IBA1 and stand out more prominently from the local background staining.

I found that the IBA1 expression in the LGN for control (2.44) and inositol (2.48) treated animals did not significantly differ ($F_{1,9} = 0.132$, ns) (Fig. 3.3F).

In their more common, ramified state, microglia have substantially more complex shapes than amoeboid microglia. Ramified microglia have numerous long branches while phagocytic cells are more rounded with few branches. My approach to measuring the complexity of the cell shape was to measure the ratio of the perimeter to area [165]. Both would be expected to be low when the microglia transition to a more rounded amoeboid shape and high in cells with longer or more numerous ramified processes or cells that are highly polarized, such as migrating cells. However, because the area of a circle increases exponentially in relation to the

radius but the perimeter increases only linearly (πr2 v. 2πr), the perimeter to area ratio will also vary with cell size, thereby confounding the interpretation. I corrected for this by dividing by the perimeter to area ratio of a circle of the same area [166]. This change ensures the metric is a purer description of the degree of ramification.

The corrected perimeter to area ratio was unchanged between control (4.943) and inositol (4.915) treated animals ($F_{1,9} = 0.095$, ns) indicating a similar degree of cell ramification or shape complexity (Fig. 3.3G).

Lastly, I measured the soma area to cell area ratio. Hoyens et al. report that this ratio more closely correlates with visual activation scores than soma size alone. In rat hippocampus and prefrontal cortex, they reported that the average Pearson's R correlation with visual grading was 0.619 for soma size and 0.855 for soma area / cell area ratio [167].

Inositol treatment had no effect on soma area / cell area ratio in our experiment (Fig. 3.3H). Somas for control animals occupied 7.37% of the total cell area, while for inositol animals the fraction was 7.32%. There was no statistically significant difference ($F_{1,9} = 0.004$, ns).

Of the four measures studied, the perimeter to area ratio was best correlated with IBA1 staining intensity (Fig. 3.3E). R2 values for control and inositol conditions were 0.157 and 0.049 respectively. The correlation was in the expected direction, with perimeter to area ratio decreasing with increased IBA1 intensity (increased activation).

All morphological data were compared using a linear mixed model to increase statistical power and reduce type 2 errors, thus avoiding missing small but significant effects. Such models have been used by others to compare neuronal morphology [168]. The linear mixed model works by taking into account the hierarchical structure of the data and utilizes all data points in the analysis rather

than only the animal averages while avoiding the problem of pseudo replication. Averaging repeated samples taken from the same animal, while statistically valid, has the disadvantage of discarding useful information about within animal variability. The results of the linear mixed model were compared with the more commonly used t-test. In all instances the conclusions were the same, there were no differences found in morphology between the control and treated animals.

3.5 Homer Puncta Size Increased in Adult V1b.

Lastly, I sought to test whether visual acuity might be improved by alterations of synaptic components further downstream in the visual pathway. I used IHC to look at several pre- and post-synaptic markers (Table 2.1) of excitatory and inhibitory neurons in the mature P35 V1. Representative images of each synaptic marker and associated puncta masks after thresholding are shown in Fig. 3.6A.

I quantified the density of immunostained puncta in layers II/III (Fig. 3.6B) and layer 5 (data not shown). For VGLUT1, a presynaptic vesicular glutamate transporter which marks mainly intracortical connections [169], control mean was 59.8 ± 8.53 puncta per high power field (hpf) and inositol mean was 58.1 ± 7.93 puncta/hpf, these density means were not significantly different ($n = 5/4$, $t = 0.137$, ns). Homer, a post-synaptic marker of excitatory glutamatergic synapses [170], was 37.7 ± 2.02 puncta/hpf for control and 37.3 ± 2.11 puncta/hpf for inositol, which were not significantly different ($n = 5/4$, $t = 0.1377$, ns).

Vesicular GABA Transporter (VGAT) control puncta had an average density of 7.55 ± 1.15 while inositol puncta density was 7.32 ± 0.72 puncta/hpf, these were not different between treatments ($n = 6/5$, $t = 0.161$, ns). Finally, the inhibitory synapse post-synaptic scaffolding protein gephyrin had average densities of 19.8 ± 1.92 for control and 20.4 ± 1.62 puncta/hpf for inositol treated which were not different ($n = 6/5$, $t = 0.243$, ns).

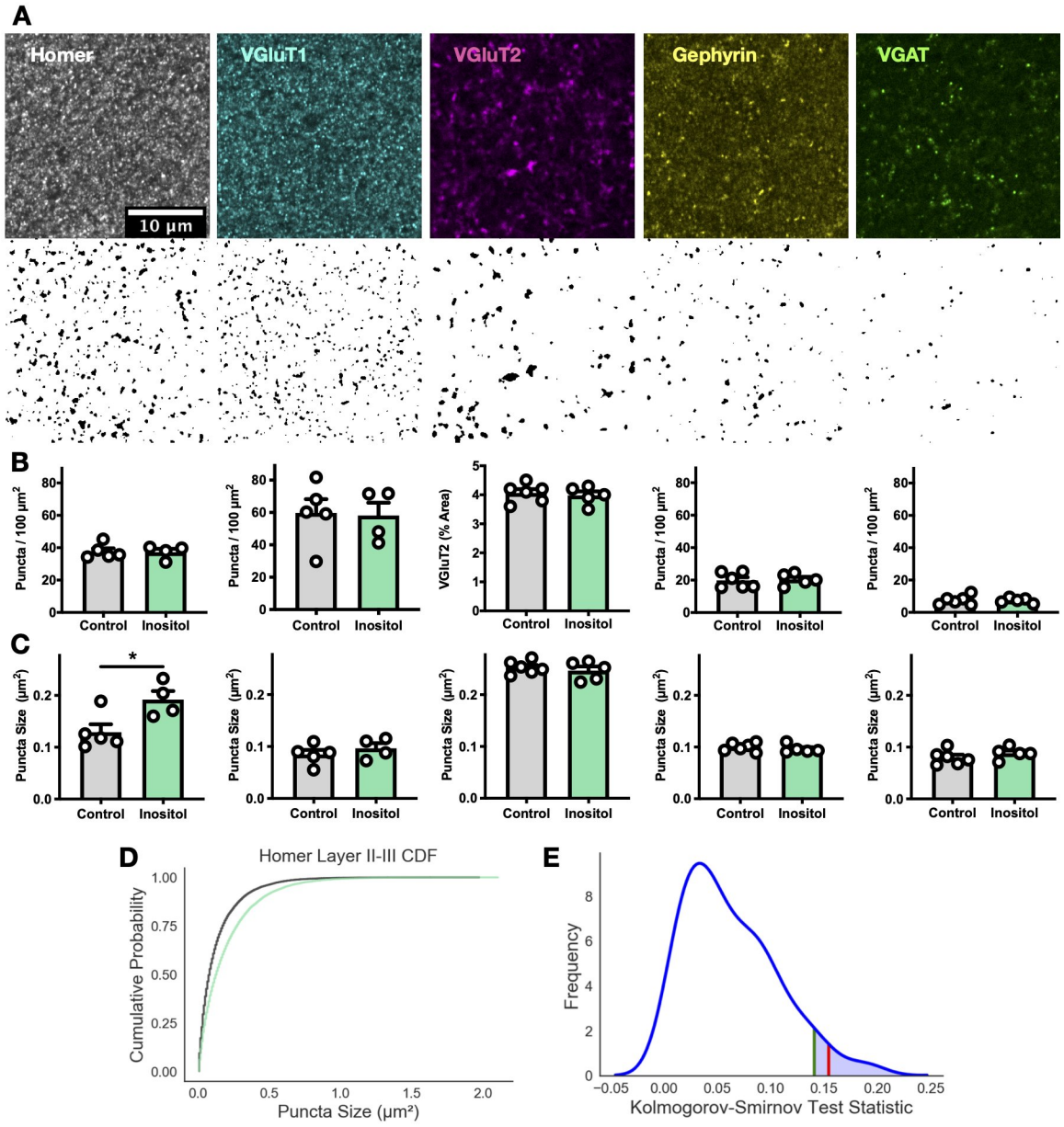

Figure 3.6: Increased size of excitatory post-synaptic puncta in mature mouse V1b. A.) Representative layer 2-3 neuropil regions from control V1b stained with antibodies to Homer, VGLUT1, VGLUT2, Gephyrin, and VGAT (left), and associated puncta masks (right). B.) Mean puncta density for each marker in control and inositol treated animals from cortical layers with most prominent staining, VGLUT2 is reported as % area (control N=6; inositol N=5). Square ROIs are taken from the neuropil. All differences are non-significant. C.) Mean puncta size from the same regions as B. (Means compared with Students t-test, * p <0.05). D.) Cumulative Distribution Frequency plot for Homer puncta size in layer 2-3 showing rightward shift. E.) Distribution of layer 2-3 Homer control versus inositol K-S test statistics from exact permutation test. 95th percentile in green, observed test statistic in red.

VGLUT2—a marker of thalamocortical projections [171, 172, 173]—percent VGLUT2 coverage was calculated as in the LGN analysis. Control animals had a mean of 4.07 ± 0.13 % coverage while inositol treated animals had a mean of 3.98 ± 0.14 % coverage. The difference was not statistically significant ($n = 6/5$, $t = 0.4523$, ns).

Additionally, I measured the densities of all the markers but VGLUT2 in cortical layer 5. Results were similar to layer 2-3 (Fig. 3.7A). In both layers, I noted that the densities of excitatory synapse markers were generally higher than those of inhibitory. This is reasonable considering that the ROIs were selected in the neuropil and avoided cell bodies and many proximal dendrites, where the majority of the inhibitory inputs would be found [174]. Overall, my data show that densities of many pre- and post-synaptic markers in primary visual cortex are not affected by inositol treatment.

Puncta size was next measured from the same set of images (Fig. 3.6C). VGLUT1 was not affected by inositol treatment ($n = 5/4$, $t = 0.897$, ns). Neither was layer 4 VGLUT2 significantly different ($n = 6/5$, $t = 0.656$, ns). However, when I examined Homer, I surprisingly found that mean puncta size was increased by 49% with inositol supplementation, from 0.129 ± 0.016 um^2 for control animals to 0.192 ± 0.017 um^2 for inositol treated ($n = 5/4$, $t = 2.764$, $^*p = 0.028$; two-tailed unpaired t-test). Inhibitory synapse markers VGAT ($n = 6/5$, $t = 1.087$, $p = 0.305$) and Gephyrin ($n = 6/5$, $t = 0.748$, ns) remained unchanged. I also quantified puncta sizes in layer 5 for VGLUT1, Homer, VGAT, and Gephyrin (Fig. 3.7B). The results were nearly identical. In summary, of the markers I examined, I found that the excitatory post-synaptic protein Homer showed a significant increase in puncta size when treated with inositol.

I considered the possibility that inositol may have an effect on the distribution of

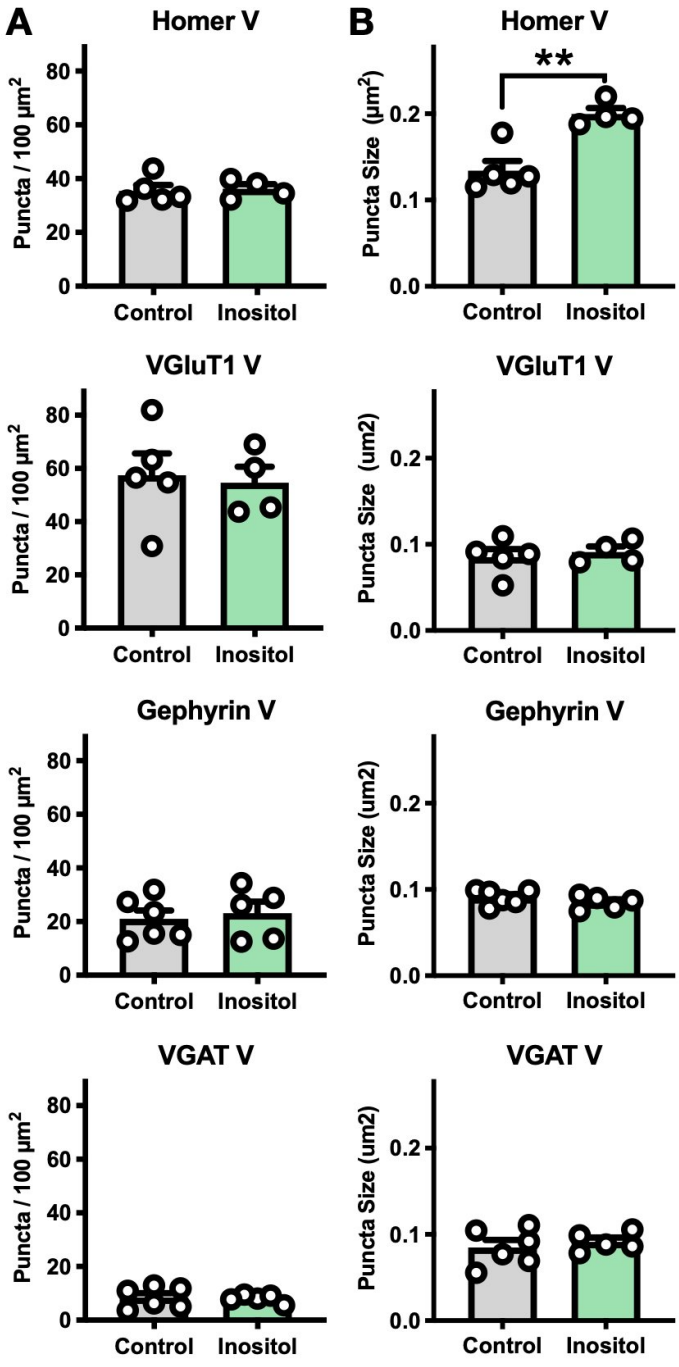

Figure 3.7: Primary visual cortex layer 5 IHC puncta size and density. A.) Puncta density for Homer, VGLUT1, Gephyrin, and VGAT. B.) Puncta size for the same markers. Means compared with unpaired two-sided t-test, ** $p = .0024$

puncta sizes, a finding that might be missed when simply comparing sample means. Many different distributions can share the same mean, leaving open the possibility that inositol may skew the distribution left or right without affecting the mean. To discover if the shape of the sample distributions was altered by inositol treatment, I employed a two-sample Kolmogorov-Smirnov test, a non-parametric test that reports the greatest vertical distance between two cumulative distribution frequencies (CDF) plots. For this analysis, the known effect on Homer puncta size served as a useful control. As expected, the Homer distribution was significantly right shifted with inositol treatment and the effect size was very pronounced (Fig. 3.6D). VGLUT1, VGAT, and Gephyrin inositol treated puncta size CDF plots did not differ from control based on visual inspection (Fig. 3.8A).

To obtain significance, I used a block-exchangeable exact permutation test [175] with the two-sample Kolmogorov-Smirnov test statistic as the dependent variable. Essentially this approach tests the null hypothesis that the treatment assignment has no predictive value and therefore randomly reassigning data points to one or the other will not affect the results. The total number of animals per experiment was 9 or 11, so I was able to do an exact test, i.e. I tested all possible permutations of data points. Because many observations came from each animal, I permuted at the animal level, the same as original treatment allocation, thereby preserving the dependent structure of the data. The only assumption of a permutation test is exchangeability, which is satisfied by keeping observations from the same animal in the same permutation block.

The empirical density distributions of test statistics for all possible permutations of Homer control and inositol data are shown (Fig. 3.6E). The observed test statistic t for the non-permuted data was 0.154 (shown in red) which was higher than the critical value representing the 95th percentile of all possible test statistics (shown in

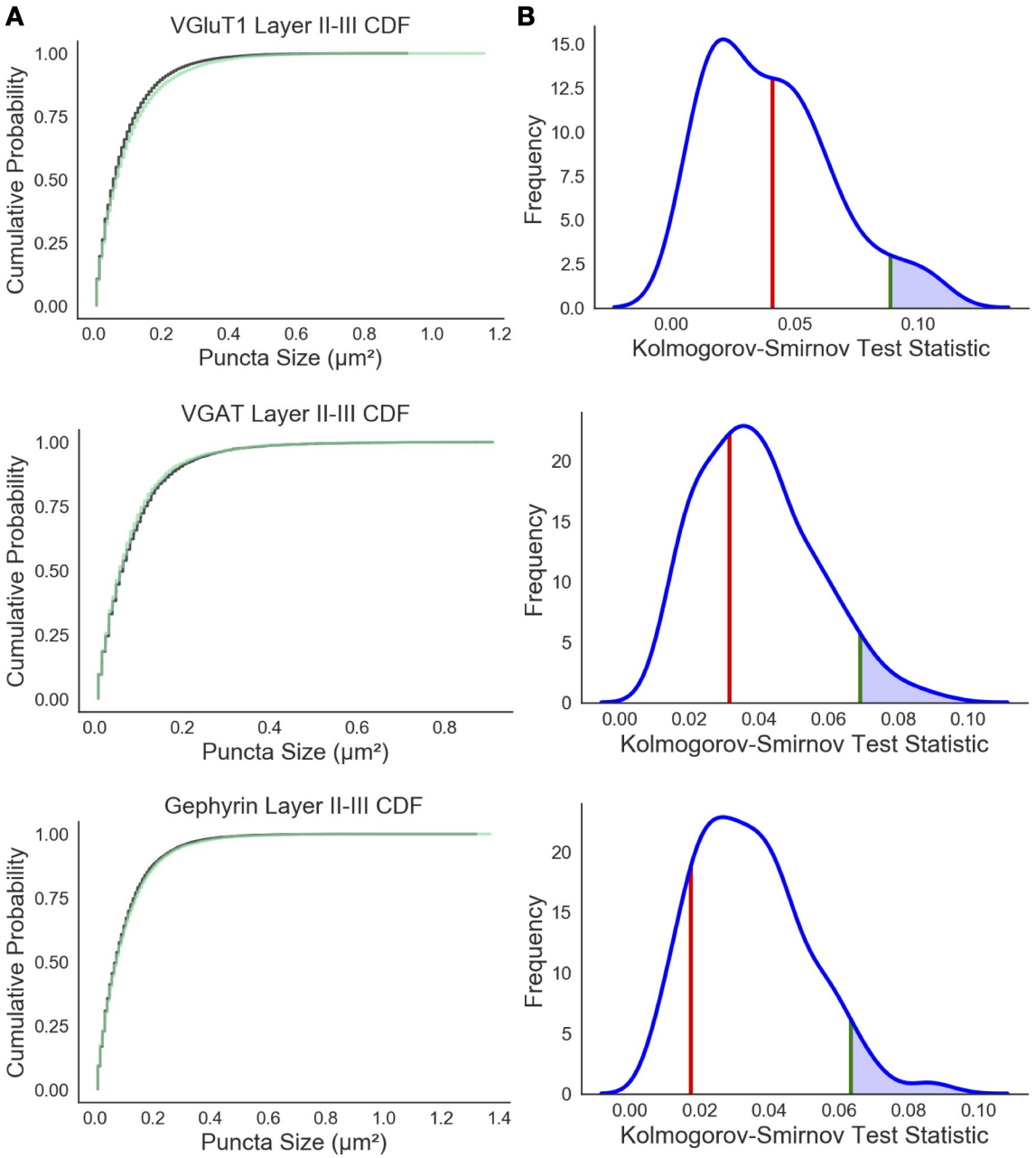

Figure 3.8: Distributions of VGLUT1, VGAT, and Gephyrin puncta size are not changed by inositol A.) Cumulative Distribution Frequency plots showing puncta sizes from control (grey) and inositol (green) treated animals. B.) Density distributions of t statistics from the exact permutation test. Observed t-statistic shown in red, critical test value shown in green.

green). The Homer test statistic in fact was greater than 96.8% of all test statistics.

Test statistic density distributions for the other markers showed no significant effect of inositol on VGLUT1 ($t = 0.041$, 53.17%), VGAT ($t = 0.031$, 33.98%), or Gephyrin ($t = 0.018$, 14.07%) (Fig. 3.8B).

As a final method to detect changes in synaptic markers, I quantified the sum of baseline subtracted pixel values in each channel within layer specific ROIs, a measure we termed CTRF. For VGLUT1, Homer, VGAT, and Gephyrin, I measured in layers II/III and V. For VGLUT2 I measured in layer 4. Inositol treatment had no effect on the CTRF for any marker in any of the layers analyzed (Fig. 3.9).

Note: All experiments and analyses for figures 3.1-9 were performed solely by the author.

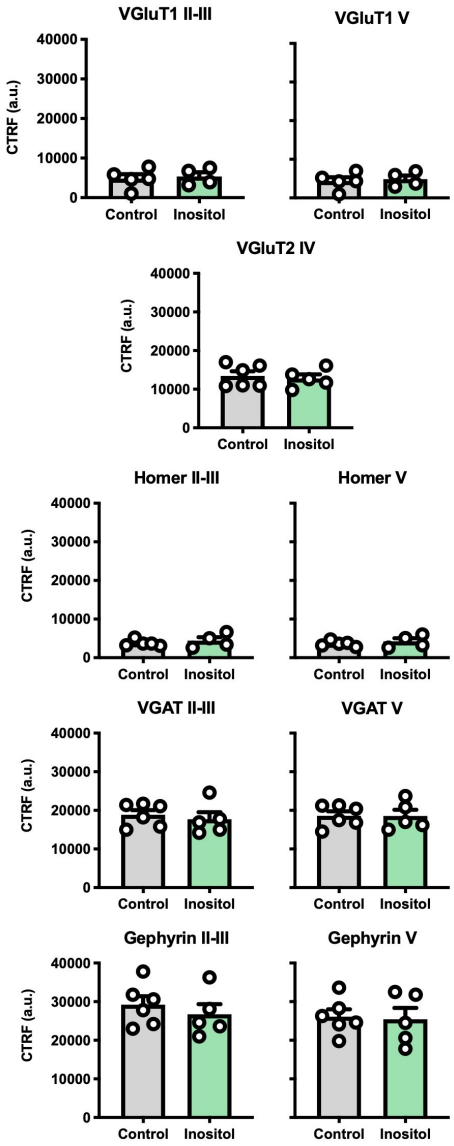

Figure 3.9: Corrected total regional fluorescence (CTRF) for synaptic markers in mature V1b is not changed. CTRF for control and inositol treated animals is compared for each synaptic marker tested in the most relevant cortical layers. None of the differences are significant. Means compared with unpaired two-tailed t-test. 5-6 animals per condition.

4 Discussion

Inositol is legally required to be included in baby formula, albeit at levels much lower than those found in human milk [176, 177]. It is thought to play a role in brain development, but the exact function is not known. My research shows that inositol can impact synapse stability and maturation perhaps by way of microglial engulfment of unwanted presynaptic terminals. To my knowledge, this is the first time that a dietary factor has been to affect synaptic pruning or connectional specificity. Whatever processes underly this effect, they appear to not be saturated with baseline levels of dietary inositol as an approximately 26% increase in dietary intake has significant cellular and functional consequences. In adults, 50% of brain inositol is produced *in situ*, while the other 50% is extracted from the blood supply, some of this being derived from diet [178]. It is not known whether the newborn brain has the same capacity for endogenous synthesis, however experiments with IMPase KO animals showed that in the absence of all endogenous inositol production dietary supplementation can protect normal brain development [179].

4.1 Delayed Effect of Inositol on dLGN Input Segregation

In my thesis work, I discovered that neonatal supplementation of myo-inositol increases segregation of eye inputs in the LGN. To the best of my knowledge, this is the first report of such an effect by a dietary factor. At P11, when segregation is normally complete, the effect is absent, but at P14 segregation is more pronounced in inositol treated animals. Why is inositol treatment associated with increased segregation at P14 but not P11? The timing coincides with eye opening and the onset of experience dependent refinement. Alternatively, the switch from stage II cholinergic retinal waves to stage III glutamatergic retinal waves could be responsible. Perhaps inositol selectively affects the pruning of glutamatergic

synapses. Inositol intake may prolong the period of input refinement, effectively delaying closing of a developmental window. Input segregation involves elimination of certain synapses and sprouting of others. I did not explore whether inositol may contribute to this latter phenomenon, but if so it would provide an alternative explanation for the increased segregation I observed.

4.2 Enhanced Microglial Engulfment Without Morphological Activation

When interpreting the data showing increased engulfment of presynaptic material by microglia in the LGN, an important caveat is that I imaged microglia from all subregions of the LGN. The density of retinal inputs is known to be higher in the shell region compared to the core [73]. Furthermore, microglia activity is probably higher in the transition region between contralateral and ipsilateral eye zones [26]. Any regional sampling differences between treated and control could therefore confound the interpretation of the results.

Increased engulfment of presynaptic inputs without a concomitant change in microglial morphology suggests that inositol may act on the neuronal compartment rather than by modifying the activation state of microglia. Perhaps it decreases stability of weak synapses or increases the stability of the stronger synapses, thus influencing the rate of removal. One possible mechanism is that inositol may alter the prevalence or distribution of molecular tags important in guiding microglia to synapses that need to be removed. One such tag, C3, is expressed in RGC terminals during the period of synaptic refinement from P5-P8 [58]. Expression of C3 is dependent on the complement initiator protein C1q. Inositol may extend the expression of C1q past P8 allowing additional time for pruning by microglia. Bialas and Schafer demonstrated that secreted TGF-β secreted from astrocytes drives RGC expression of C1q [60]. Inositol deficient diets have been shown to decrease mRNA expression of TGF-β in the intestine of young grass carp [180]. It is

therefore intriguing to think that inositol supplementation may increase TGF-β in astrocytes thereby upregulating expression of C1q and C3, but this hypothesis has yet to be tested.

Inositol is also the precursor of certain important second messengers and signaling molecules. For example, upon insulin binding to insulin receptor (IR), adaptor proteins such as insulin receptor substrate 1 and 2 (IRS1/2) are recruited to the membrane and tyrosine phosphorylated [181, 182]. These phospho-proteins bind the SH2 domain of phosphatidylinositol-3-kinase (PI3K) which then phosphorylates the 3-carbon of PIP2 and generating PIP3 [183]. PIP3 recruits Akt to the membrane where it is activated by Phosphoinositide-Dependent Kinase-1 (PDK1) [184, 183]. This enables GLUT4 to be targeted to the membrane so it can lower extracellular glucose [115]. PIP2 can also be cleaved by phospholipase C (PLC) to generate diacylglycerol (DAG) and inositol 1,4,5-triphosphate (IP3) [185] and release intracellular Ca^{2+} stores from the ER [186, 187, 188]. Inositol is also necessary for synthesis of glycosylphosphatidylinositol (GPI) anchors which tether many proteins to the cell membrane, including ephrins and Eph receptors which instruct rought retinotopic mapping.

If expression of synapse removal signals is contingent on pathways that contain inositol derivatives, additional inositol may increase activation of these pathways. Therefore, one future direction I would like to pursue is to look at whether regulation of C1q, C3, TGF-β or C3R utilizes any of the inositol derivates described above and whether the inositol containing molecules might be rate limiting.

Although I consider it more likely that inositol affects a change in neurons, it remains possible that the microglia are altered instead, despite the lack of a morphological correlate. For instance, inositol may increase the expression of CR3 (CD11b) by microglia, which could lead to increased engulfment. I did not measure

CR3 in this study, but it would be interesting to see whether inositol changes its expression levels.

4.3 Increased Engulfment Does Not Change dLGN VGLUT2 Density

As noted previously, VGLUT2, a presynaptic marker of excitatory glutamatergic synapses in the retino-geniculate-cortical pathway was not changed in the LGN with inositol treatment. Similarly, I found no difference in VGLUT2 in the adult V1b. How does microglial pruning affect the local synaptic landscape? Schafer et al found a 50% decrease in engulfment at P5 was associated with an 80% increase in VGLUT2 density and a 30% increase in VGLUT2/GluR1 density [62]. Curiously, my results did not show the expected decrease in VGLUT2 density even though microglial engulfment was increased. Several differences may serve to explain this seeming disparity. Schafer et al used array tomography whereas I relied on confocal microscopy which has a lower resolution. The relationship between microglial engulfment and VGLUT2 may also not be strictly linear. Whereas the Schafer lab found a decrease in engulfment led to increased VGLUT2 this does not guarantee that an increase in engulfment would lead to the opposite. Furthermore, the method used to quantify density was different. Rather than reporting number of puncta per area, I used percent area as my measure of density. The tendency of VGLUT2 puncta to cluster together makes separating individual puncta difficult or impossible. Schafer et al later adopted this method as well [156]. If increased pruning leads to fewer VGLUT2+ puncta but these remaining puncta are larger it would also not change the percent area covered. Are the spared synapses enlarged by the elimination of their siblings? Answering this question will require higher resolution imaging to adequately separate individual inputs from VGLUT2 clusters.

Alternatively, it is possible that engulfed material in the microglia does not represent RGC boutons, but is instead axonal material. Refinements to the axonal

arbor occur during the first postnatal week, concomitant with cholinergic retinal waves. Segregation of eye specific inputs is partially a result of the removal of axon branches that have overshot their target. The additional engulfed material could be axons in the process of being removed or cleaned up following this process rather than terminals. This would explain why the density of VGLUT2 does not change. I do not believe that this is the case though, as CTB has previously been shown to label axon terminals more robustly than axon shafts [73]. However, in future studies, we plan to co-stain for VGLUT2 and IBA1 and quantify the engulfed VGLUT2 to definitively address this issue.

4.4 Implications of Increased V1b Homer Puncta Size

While VGLUT2 was not found to be changed, to my surprise the post-synaptic side, marked with Homer, was enlarged in adult primary visual cortex. Larger synapses are associated with increases in synaptic strength [189]. I attempted to stain for Homer in the LGN as well, but technical hurdles prevented reliable quantification. The Homer finding is significant as well because it overlaps with the age at which we measured visual acuity thereby providing a possible explanation for the improvement in visual function following inositol treatment.

There are three Homer isoforms, each with several splice variants. For Homer1, the N-terminal truncated Homer1a splice variant is activity dependent whereas the longer Homer1b and Homer1c form tetramers that are negatively regulated by Homer1a expression. Recently, Homer1a has been shown to be elevated following certain treatments for depression [190]. If the increase in Homer in the V1b reflects an increase in the activity dependent antagonist Homer1a it may have implications for treatment of mood disorders. Importantly, other mood altering pharmaceuticals such as Lithium [191] and Valproate (VPA) have been shown to modify inositol levels, further pointing to a linkage between inositol and mood. Valproic Acid has

been shown to inhibit the enzyme MIPS that catalyzes the formation of myo-inositol phosphate from G6P [192]. On the other hand, Homer1b/c has been shown to couple group I metabotropic glutamate receptors (mGluR1/5) to IP3/Ca^{2+} signaling in neurons [193, 194] and is upregulated by VPA and Lithium treatment [195]. My Homer antibody targets the shared N-terminal and so does not differentiate between splice variants, but regardless of which variant is upregulated, the potential linkage to mood disorders is intriguing to say the least and warrants further investigation.

4.5 Source of Increased Visual Acuity

How do changes in the LGN and primary visual cortex lead to increased visual acuity in adult animals? The upper limit of visual acuity is determined by the density of photoreceptor cells in the fovea. However, visual acuity continues to increase after retinal development is completed. The refinement of receptive fields in the thalamus and cortex are responsible for these later improvements. Receptive fields are sharpened as convergence increases and as local inhibitory circuits mature. One of the ways that retinal convergence increases is by elimination of specific superfluous synapses. I have shown that inositol increases segregation of eye specific inputs in the LGN, which may be correlated with an increased retinotopic refinement as well, though this has not been directly shown.

Development of visual acuity is not strictly dependent on visual experience, as chronically dark reared mice will reach the same visual acuity as light reared animals, albeit with a significant delay [14]. This indicates that visual acuity can develop by way of a feedforward mechanism. In this case, the traditional model whereby thalamic refinement precedes and informs cortical circuit maturation may hold true. Spatial visual acuity improves as receptive fields in the LGN and cortex are sharpened. The time frame for this process overlaps with the third phase of retinogeniculate refinement during which retinal convergence decreases drastically

and the few remaining functional inputs are substantially strengthened. Retinotopy of the LGN may then be propagated to the cortex.

4.6 Limitations

I did not look at the density of RGCs in the retina. It's possible that inositol affects this number, especially given that microglia have been shown to engulf whole RGCs during neurogenesis in the retina. A change in the total number of inputs to the LGN might influence the degree of input segregation, VGLUT2 density, or retinal terminal engulfment. Retinal whole mounts are frequently used to count the number of RGCs, but this has yet to be done.

My data would be bolstered by the inclusion of additional timepoints, particularly by matching timepoints across experiments. Specifically, the microglial morphology and engulfment were only assessed at P8, while the segregation and VGLUT2 density in the LGN was measured later at P11 and P14. The relationship between engulfment and input segregation may become clearer if both metrics were quantified between P8 and P14. Furthermore, microglial synaptophagy peaks at P5, and is largely completed by P10. Some activity remains at P8, but adding an earlier P5 timepoint might show a more significant effect of inositol.

Criteria for the selection of ROIs could be more robust. As mentioned, there are known differences between the shell and core regions of the LGN in terms of retinal terminal density. Microglia imaged for the engulfment experiment came from all parts of the LGN, though the degree of synapse elimination is regionally variable. Any unintentional differences in the regional distribution of sampled microglia may complicate the interpretation of the engulfment.

In lieu of some controls, I relied on comparisons with published data to confirm that my methods were working correctly. For example, the engulfment fraction of control

microglia was noted closely match that published by Schafer et al., but internal controls to confirm that the imaging and analysis were properly carried would be preferable. Minocycline could have been used to block microglial phagocytosis, and confirming that the observed engulfed material does not represent a false positive.

4.7 Future Directions

Retinogeniculate and thalamocortical projections synapse onto both excitatory and inhibitory neurons in the thalamus and V1, but this study did not distinguish between cell type when quantifying synapses. Maturation of inhibitory circuitry is an important contributor to the refinement of receptive fields and the development of visual acuity [196]. The three major classes of inhibitory interneurons differ in the subcellular localization of their axons. PV+ interneurons form synapses on pyramidal cell somas and proximal dendrites while SST and VIP cells synapse on distal dendrites. In my analysis of synaptic markers in V1, I avoided cell bodies when outlining ROIs. My measurements of the pre-synaptic inhibitory marker VGAT can therefore be assumed to be biased towards VIP and SST projections, with a paucity of PV projections. Future experiments might measure VGAT signal adjacent to cell somas to focus on the contribution of PV+ inhibitory neurons. Immunostaining with PV and gephyrin could be used to see if the thalamocortical projections to inhibitory neurons are differentially altered.

Though we saw no change in microglial morphology, perhaps this is unsurprising, given that others have reported classical microglial activation is not required for their role in developmental synaptic pruning [197]. Repeating these two experiments using mice treated with minocycline would test whether the increase in microglial phagocytosis is responsible for the observed increased segregation. Minocycline prevents microglial activation including non-canonical activation that is responsible for synaptophagy [198].

Inositol is the building block of glycosylphosphatidylinositol anchored proteins, but whether additional inositol impacts the availability of GPI anchors has not been determined. Many synaptic adhesion molecules, such as LRRTMs, Neuroligins, and T-Cadherin are GPI-APs. It would be interesting to test in future experiments whether inositol treatment alters the cell surface expression of these proteins.

4.8 Conclusions

In this study I found surprising new roles for inositol in enhancing input segregation and microglial phagocytosis, enlarging excitatory post-synaptic Homer puncta, and improving visual acuity in adult mice. Inositol is considered safe for human consumption and is already being investigated as a therapy for gestational diabetes. My data suggest that humanizing infant formula with physiological levels of inositol may help improve neurological development outcomes in formula fed children. More research is recommended to better understand the specific effects and the underlying mechanisms.

5 Bibliography

[1] Arthur I Eidelman and Richard J Schanler. "Breastfeeding and the use of human milk." In: *Pediatrics* (2012).

[2] American Academy of Pediatrics et al. "Breastfeeding and maternal and infant health outcomes in developed countries". In: *AAP Grand Rounds* 18.2 (2007), pp. 15–16.

[3] Beatrice E Carbone et al. "Synaptic Connectivity and Cortical Maturation Are Promoted by the ω-3 Fatty Acid Docosahexaenoic Acid". In: *Cerebral Cortex* (2019).

[4] Louise Muscat et al. "Crossed and uncrossed retinal projections to the hamster circadian system". In: *Journal of Comparative Neurology* 466.4 (2003), pp. 513–524.

[5] Xu-ying Ji et al. "Thalamocortical innervation pattern in mouse auditory and visual cortex: laminar and cell-type specificity". In: *Cerebral Cortex* 26.6 (2015), pp. 2612–2625.

[6] Wenzhi Sun et al. "Thalamus provides layer 4 of primary visual cortex with orientation-and direction-tuned inputs". In: *Nature neuroscience* 19.2 (2016), p. 308.

[7] Y Kate Hong et al. "Refinement of the retinogeniculate synapse by bouton clustering". In: *Neuron* 84.2 (2014), pp. 332–339.

[8] Michelle Kloc and Arianna Maffei. "Target-specific properties of thalamocortical synapses onto layer 4 of mouse primary visual cortex". In: *Journal of Neuroscience* 34.46 (2014), pp. 15455–15465.

[9] Jun Zhuang et al. "Layer 4 in primary visual cortex of the awake rabbit: contrasting properties of simple cells and putative feedforward inhibitory interneurons". In: *Journal of Neuroscience* 33.28 (2013), pp. 11372–11389.

[10] Derek Bowie and Mark L Mayer. "Inward rectification of both AMPA and kainate subtype glutamate receptors generated by polyamine-mediated ion channel block". In: *Neuron* 15.2 (1995), pp. 453–462.

[11] Zsuzsanna Almasi et al. "Distribution patterns of three molecularly defined classes of GABAergic neurons across columnar compartments in mouse barrel cortex". In: *Frontiers in neuroanatomy* 13 (2019), p. 45.

[12] Carsten K Pfeffer et al. "Inhibition of inhibition in visual cortex: the logic of connections between molecularly distinct interneurons". In: *Nature neuroscience* 16.8 (2013), p. 1068.

[13] F Hajos et al. "Geniculo-cortical afferents form synaptic contacts with vasoactive intestinal polypeptide (VIP) immunoreactive neurons of the rat visual cortex". In: *Neuroscience letters* 228.3 (1997), pp. 179–182.

[14] Erin Kang et al. "Visual acuity development and plasticity in the absence of sensory experience". In: *Journal of Neuroscience* 33.45 (2013), pp. 17789–17796.

[15] William Guido. "Refinement of the retinogeniculate pathway". In: *The Journal of Physiology* 586.18 (2008), pp. 4357–4362.

[16] Roger W Sperry. “Chemoaffinity in the orderly growth of nerve fiber patterns and connections”. In: *Proceedings of the National Academy of Sciences* 50.4 (1963), pp. 703–710.

[17] Todd McLaughlin and Dennis DM O’Leary. “Molecular gradients and development of retinotopic maps”. In: *Annu. Rev. Neurosci.* 28 (2005), pp. 327–355.

[18] Cory Pfeiffenberger et al. “Ephrin-As and neural activity are required for eye-specific patterning during retinogeniculate mapping”. In: *Nature neuroscience* 8.8 (2005), pp. 1022–1027.

[19] Robert Hindges et al. “EphB forward signaling controls directional branch extension and arborization required for dorsal-ventral retinotopic mapping”. In: *Neuron* 35.3 (2002), pp. 475–487.

[20] Andrew D Huberman, Marla B Feller, and Barbara Chapman. “Mechanisms underlying development of visual maps and receptive fields”. In: *Annu. Rev. Neurosci.* 31 (2008), pp. 479–509.

[21] Lynda Erskine and Eloisa Herrera. “Connecting the retina to the brain”. In: *ASN neuro* 6.6 (2014), p. 1759091414562107.

[22] Charlene A Ellsworth et al. “Ephrin-A2 and-A5 influence patterning of normal and novel retinal projections to the thalamus: Conserved mapping mechanisms in visual and auditory thalamic targets”. In: *Journal of Comparative Neurology* 488.2 (2005), pp. 140–151.

[23] Pierre Godement, Josselyne Salaün, and Michel Imbert. “Prenatal and postnatal development of retinogeniculate and retinocollicular projections in the mouse”. In: *Journal of Comparative Neurology* 230.4 (1984), pp. 552–575.

[24] Cory Pfeiffenberger, Jena Yamada, and David A Feldheim. “Ephrin-As and patterned retinal activity act together in the development of topographic maps in the primary visual system”. In: *Journal of Neuroscience* 26.50 (2006), pp. 12873–12884.

[25] Andrew D Huberman et al. “Ephrin-As mediate targeting of eye-specific projections to the lateral geniculate nucleus”. In: *Nature neuroscience* 8.8 (2005), p. 1013.

[26] Lisa Jaubert-miazza et al. “Structural and functional composition of the developing retinogeniculate pathway in the mouse”. In: *Visual neuroscience* 22.5 (2005), pp. 661–676.

[27] Marla B Feller et al. “Requirement for cholinergic synaptic transmission in the propagation of spontaneous retinal waves”. In: *Science* 272.5265 (1996), pp. 1182–1187.

[28] Rachel OL Wong. “Retinal waves and visual system development”. In: *Annual review of neuroscience* 22.1 (1999), pp. 29–47.

[29] Jay Demas, Stephen J Eglen, and Rachel OL Wong. “Developmental loss of synchronous spontaneous activity in the mouse retina is independent of visual experience”. In: *Journal of Neuroscience* 23.7 (2003), pp. 2851–2860.

[30] Christine L Torborg and Marla B Feller. “Spontaneous patterned retinal activity and the refinement of retinal projections”. In: *Progress in neurobiology* 76.4 (2005), pp. 213–235.

[31] Anu Bansal et al. “Mice lacking specific nicotinic acetylcholine receptor subunits exhibit dramatically altered spontaneous activity patterns and reveal a limited role for retinal waves in forming ON and OFF circuits in the inner retina”. In: *Journal of Neuroscience* 20.20 (2000), pp. 7672–7681.

[32] Anna A Penn et al. “Competition in retinogeniculate patterning driven by spontaneous activity”. In: *Science* 279.5359 (1998), pp. 2108–2112.

[33] Ji-jian Zheng, Seunghoon Lee, and Z Jimmy Zhou. “A developmental switch in the excitability and function of the starburst network in the mammalian retina”. In: *Neuron* 44.5 (2004), pp. 851–864.

[34] Francesco Mattia Rossi et al. “Requirement of the nicotinic acetylcholine receptor $\beta 2$ subunit for the anatomical and functional development of the visual system”. In: *Proceedings of the National Academy of Sciences* 98.11 (2001), pp. 6453–6458.

[35] Ben K Stafford et al. “Spatial-temporal patterns of retinal waves underlying activity-dependent refinement of retinofugal projections”. In: *Neuron* 64.2 (2009), pp. 200–212.

[36] Fu-Sun Lo, Jokubas Ziburkus, and William Guido. “Synaptic mechanisms regulating the activation of a Ca2+-mediated plateau potential in developing relay cells of the LGN”. In: *Journal of neurophysiology* 87.3 (2002), pp. 1175–1185.

[37] Jon M Kornhauser et al. “CREB transcriptional activity in neurons is regulated by multiple, calcium-specific phosphorylation events”. In: *Neuron* 34.2 (2002), pp. 221–233.

[38] Steven Finkbeiner et al. “CREB: a major mediator of neuronal neurotrophin responses”. In: *Neuron* 19.5 (1997), pp. 1031–1047.

[39] Daniel A Butts, Patrick O Kanold, and Carla J Shatz. “A burst-based “Hebbian” learning rule at retinogeniculate synapses links retinal waves to activity-dependent refinement”. In: *PLoS biology* 5.3 (2007), e61.

[40] Paul A Yates et al. “Computational modeling of retinotopic map development to define contributions of EphA-ephrinA gradients, axon-axon interactions, and patterned activity”. In: *Journal of neurobiology* 59.1 (2004), pp. 95–113.

[41] Lisa Bjartmar et al. “Neuronal pentraxins mediate synaptic refinement in the developing visual system”. In: *Journal of Neuroscience* 26.23 (2006), pp. 6269–6281.

[42] Chinfei Chen and Wade G Regehr. “Developmental remodeling of the retinogeniculate synapse”. In: *Neuron* 28.3 (2000), pp. 955–966.

[43] Michael Howarth, Lauren Walmsley, and Timothy M Brown. “Binocular integration in the mouse lateral geniculate nuclei”. In: *Current Biology* 24.11 (2014), pp. 1241–1247.

[44] Jianhua Cang et al. “Development of precise maps in visual cortex requires patterned spontaneous activity in the retina”. In: *Neuron* 48.5 (2005), pp. 797–809.

[45] D Stellwagen and CJ Shatz. "An instructive role for retinal waves in the development of retinogeniculate connectivity". In: *Neuron* 33.3 (2002), pp. 357–367.
[46] Aaron G Blankenship et al. "Synaptic and extrasynaptic factors governing glutamatergic retinal waves". In: *Neuron* 62.2 (2009), pp. 230–241.
[47] Alessandro Maccione et al. "Following the ontogeny of retinal waves: pan-retinal recordings of population dynamics in the neonatal mouse". In: *The Journal of physiology* 592.7 (2014), pp. 1545–1563.
[48] Daniel Kerschensteiner. "Glutamatergic retinal waves". In: *Frontiers in neural circuits* 10 (2016), p. 38.
[49] Bryan M Hooks and Chinfei Chen. "Distinct roles for spontaneous and visual activity in remodeling of the retinogeniculate synapse". In: *Neuron* 52.2 (2006), pp. 281–291.
[50] Shane R Crandall, Scott J Cruikshank, and Barry W Connors. "A corticothalamic switch: controlling the thalamus with dynamic synapses". In: *Neuron* 86.3 (2015), pp. 768–782.
[51] RW Guillery and S Murray Sherman. "Thalamic relay functions and their role in corticocortical communication: generalizations from the visual system". In: *Neuron* 33.2 (2002), pp. 163–175.
[52] S Murray Sherman and RW Guillery. "The role of the thalamus in the flow of information to the cortex". In: *Philosophical Transactions of the Royal Society of London. Series B: Biological Sciences* 357.1428 (2002), pp. 1695–1708.
[53] Dwayne W Godwin et al. "Ultrastructural localization suggests that retinal and cortical inputs access different metabotropic glutamate receptors in the lateral geniculate nucleus". In: *Journal of Neuroscience* 16.24 (1996), pp. 8181–8192.
[54] Robert T Fremeau et al. "Vesicular glutamate transporters 1 and 2 target to functionally distinct synaptic release sites". In: *Science* 304.5678 (2004), pp. 1815–1819.
[55] Andrew D Thompson et al. "Cortical feedback regulates feedforward retinogeniculate refinement". In: *Neuron* 91.5 (2016), pp. 1021–1033.
[56] Jean-Pierre Sommeijer et al. "Thalamic inhibition regulates critical-period plasticity in visual cortex and thalamus". In: *Nature neuroscience* 20.12 (2017), pp. 1715–1721.
[57] Juliane Jaepel et al. "Lateral geniculate neurons projecting to primary visual cortex show ocular dominance plasticity in adult mice". In: *Nature neuroscience* 20.12 (2017), p. 1708.
[58] Beth Stevens et al. "The classical complement cascade mediates CNS synapse elimination". In: *Cell* 131.6 (2007), pp. 1164–1178.
[59] Linda J Lawson et al. "Heterogeneity in the distribution and morphology of microglia in the normal adult mouse brain". In: *Neuroscience* 39.1 (1990), pp. 151–170.

[60] Allison R Bialas and Beth Stevens. "TGF-β signaling regulates neuronal C1q expression and developmental synaptic refinement". In: *Nature neuroscience* 16.12 (2013), p. 1773.

[61] Larry C Katz and Carla J Shatz. "Synaptic activity and the construction of cortical circuits". In: *Science* 274.5290 (1996), pp. 1133–1138.

[62] Dorothy P Schafer et al. "Microglia sculpt postnatal neural circuits in an activity and complement-dependent manner". In: *Neuron* 74.4 (2012), pp. 691–705.

[63] Laetitia Weinhard et al. "Microglia remodel synapses by presynaptic trogocytosis and spine head filopodia induction". In: *Nature communications* 9.1 (2018), p. 1228.

[64] Richard J O'Brien et al. "Synaptic clustering of AMPA receptors by the extracellular immediate-early gene product Narp". In: *Neuron* 23.2 (1999), pp. 309–323.

[65] Gene S Huh et al. "Functional requirement for class I MHC in CNS development and plasticity". In: *Science* 290.5499 (2000), pp. 2155–2159.

[66] Kyungmin Ji et al. "Microglia actively regulate the number of functional synapses". In: *PloS one* 8.2 (2013), e56293.

[67] Santiago B Rompani et al. "Different modes of visual integration in the lateral geniculate nucleus revealed by single-cell-initiated transsynaptic tracing". In: *Neuron* 93.4 (2017), pp. 767–776.

[68] Aboozar Monavarfeshani et al. "LRRTM1 underlies synaptic convergence in visual thalamus". In: *elife* 7 (2018), e33498.

[69] Elizabeth Y Litvina and Chinfei Chen. "Functional convergence at the retinogeniculate synapse". In: *Neuron* 96.2 (2017), pp. 330–338.

[70] J Hamori, P Pasik, and T Pasik. "Different types of synaptic triads in the monkey dorsal lateral geniculate nucleus." In: *Journal fur Hirnforschung* 32.3 (1991), pp. 369–379.

[71] James E Hamos et al. "Synaptic connectivity of a local circuit neurone in lateral geniculate nucleus of the cat". In: *Nature* 317.6038 (1985), p. 618.

[72] Jose A Rafols and Facundo Valverde. "The structure of the dorsal lateral geniculate nucleus in the mouse. A Golgi and electron microscopic study". In: *Journal of Comparative Neurology* 150.3 (1973), pp. 303–331.

[73] Sarah Hammer et al. "Nuclei-specific differences in nerve terminal distribution, morphology, and development in mouse visual thalamus". In: *Neural development* 9.1 (2014), p. 16.

[74] Josh Lyskowski Morgan et al. "The fuzzy logic of network connectivity in mouse visual thalamus". In: *Cell* 165.1 (2016), pp. 192–206.

[75] VM Montero. "A quantitative study of synaptic contacts on interneurons and relay cells of the cat lateral geniculate nucleus". In: *Experimental Brain Research* 86.2 (1991), pp. 257–270.

[76] Martha E Bickford et al. "Synaptic development of the mouse dorsal lateral geniculate nucleus". In: *Journal of Comparative Neurology* 518.5 (2010), pp. 622–635.

[77] Pushpalatha PN Murthy. “Structure and nomenclature of inositol phosphates, phosphoinositides, and glycosylphosphatidylinositols”. In: *Biology of Inositols and Phosphoinositides*. Springer, 2006, pp. 1–19.

[78] Mark P Thomas, Stephen J Mills, and Barry VL Potter. “The “Other” Inositols and Their Phosphates: Synthesis, Biology, and Medicine (with Recent Advances in myo-Inositol Chemistry)”. In: *Angewandte Chemie International Edition* 55.5 (2016), pp. 1614–1650.

[79] Théodore Posternak. “Recherches dans la série des cyclites VI. Sur la configuration de la méso-inosite, de la scyllite et d’un inosose obtenu par voie biochimique (scyllo-ms-inosose)”. In: *Helvetica Chimica Acta* 25.4 (1942), pp. 746–752.

[80] Simone Garzon, Antonio Simone Laganà, and Giovanni Monastra. “Risk of reduced intestinal absorption of myo-inositol caused by D-chiro-inositol or by glucose transporter inhibitors”. In: *Expert opinion on drug metabolism & toxicology* 15.9 (2019), pp. 697–703.

[81] Ratnam S Seelan et al. “Identification of myo-Inositol-3-phosphate Synthase Isoforms CHARACTERIZATION, EXPRESSION, AND PUTATIVE ROLE OF A 16-kDa γc ISOFORM”. In: *Journal of Biological Chemistry* 284.14 (2009), pp. 9443–9457.

[82] A Lahiri Majumder and BB Biswas. *Biology of inositols and phosphoinositides*. Vol. 39. Springer Science & Business Media, 2006.

[83] Heidi Villalba et al. “Potential role of myo-inositol to improve ischemic stroke outcome in diabetic mouse”. In: *Brain research* 1699 (2018), pp. 166–176.

[84] Linying Guo et al. “Metabolic Alterations Within the Primary Visual Cortex in Early Open-angle Glaucoma Patients: A Proton Magnetic Resonance Spectroscopy Study”. In: *Journal of glaucoma* 27.12 (2018), pp. 1046–1051.

[85] William F Naccarato and William W Wells. “Identification of 6-O-β-D-galactopyranosyl myo-inositol: A new form of myo-inositol in mammals”. In: *Biochemical and biophysical research communications* 57.4 (1974), pp. 1026–1031.

[86] RMC Dawson and N Freinkel. “The distribution of free mesoinositol in mammalian tissues, including some observations on the lactating rat”. In: *Biochemical Journal* 78.3 (1961), p. 606.

[87] RS Clements Jr. “The metabolism of myo-inositol by the human kidney”. In: *J. Lab. Clin. Med.* 93 (1979), pp. 210–219.

[88] Bruce J Holub. “Metabolism and function of myo-inositol and inositol phospholipids”. In: *Annual review of nutrition* 6.1 (1986), pp. 563–597.

[89] Rex S Clements Jr and Betty Darnell. “Myo-inositol content of common foods: development of a high-myo-inositol diet”. In: *The American Journal of Clinical Nutrition* 33.9 (1980), pp. 1954–1967.

[90] Ulrich Schlemmer et al. “Phytate in foods and significance for humans: food sources, intake, processing, bioavailability, protective role and analysis”. In: *Molecular nutrition & food research* 53.S2 (2009), S330–S375.

[91] Simona Dinicola et al. “Nutritional and acquired deficiencies in inositol bioavailability. Correlations with metabolic disorders”. In: *International journal of molecular sciences* 18.10 (2017), p. 2187.
[92] RS Goodhart. “Bioflavonoids”. In: *Modern Nutrition in Health and Disease* (1973), pp. 259–267.
[93] K Hager et al. “Kinetics and specificity of the renal Na+/myo-inositol cotransporter expressed in Xenopus oocytes”. In: *The Journal of membrane biology* 143.2 (1995), pp. 103–113.
[94] H Moo Kwon et al. “Cloning of the cDNa for a Na+/myo-inositol cotransporter, a hypertonicity stress protein.” In: *Journal of Biological Chemistry* 267.9 (1992), pp. 6297–6301.
[95] J Matskevitch et al. “Effect of extracellular pH on the myo-inositol transporter SMIT expressed in Xenopus oocytes”. In: *Pflügers Archiv* 436.6 (1998), pp. 854–857.
[96] Marc Uldry et al. “Identification of a mammalian H+-myo-inositol symporter expressed predominantly in the brain”. In: *The EMBO Journal* 20.16 (2001), pp. 4467–4477.
[97] Beate Lubrich et al. “Differential expression, activity and regulation of the sodium/myo-inositol cotransporter in astrocyte cultures from different regions of the rat brain”. In: *Neuropharmacology* 39.4 (2000), pp. 680–690.
[98] Karim Lahjouji et al. “Expression and functionality of the Na+/myo-inositol cotransporter SMIT2 in rabbit kidney”. In: *Biochimica et Biophysica Acta (BBA)-Biomembranes* 1768.5 (2007), pp. 1154–1159.
[99] Michael J Coady et al. “Identification of a novel Na+/myo-inositol cotransporter”. In: *Journal of Biological Chemistry* 277.38 (2002), pp. 35219–35224.
[100] BT Hinton, RW White, and BP Setchell. “Concentrations of myo-inositol in the luminal fluid of the mammalian testis and epididymis”. In: *Reproduction* 58.2 (1980), pp. 395–399.
[101] Thomas Michaelis et al. “Identification of scyllo-inositol in proton NMR spectra of human brain in vivo”. In: *NMR in Biomedicine* 6.1 (1993), pp. 105–109.
[102] Nicholas DE Greene and Andrew J Copp. “Inositol prevents folate-resistant neural tube defects in the mouse”. In: *Nature medicine* 3.1 (1997), p. 60.
[103] Nadine Girard et al. “MRS of normal and impaired fetal brain development”. In: *European journal of radiology* 57.2 (2006), pp. 217–225.
[104] Roland Kreis, Thomas Ernst, and Brian D Ross. “Development of the human brain: in vivo quantification of metabolite and water content with proton magnetic resonance spectroscopy”. In: *Magnetic Resonance in Medicine* 30.4 (1993), pp. 424–437.
[105] Erika Brighina et al. “Human fetal brain chemistry as detected by proton magnetic resonance spectroscopy”. In: *Pediatric neurology* 40.5 (2009), pp. 327–342.
[106] Roland Kreis et al. “Brain metabolite composition during early human brain development as measured by quantitative in vivo 1H magnetic resonance

spectroscopy". In: *Magnetic Resonance in Medicine: An Official Journal of the International Society for Magnetic Resonance in Medicine* 48.6 (2002), pp. 949–958.

[107] Petra JW Pouwels et al. "Regional age dependence of human brain metabolites from infancy to adulthood as detected by quantitative localized proton MRS". In: *Pediatric research* 46.4 (1999), p. 474.

[108] Nobuo Kato. "Dependence of long-term depression on postsynaptic metabotropic glutamate receptors in visual cortex." In: *Proceedings of the National Academy of Sciences* 90.8 (1993), pp. 3650–3654.

[109] Nobuyuki Sasakawa, Mohammed Sharif, and Michael R Hanley. "Metabolism and biological activities of inositol pentakisphosphate and inositol hexakisphosphate". In: *Biochemical pharmacology* 50.2 (1995), pp. 137–146.

[110] Susan M Voglmaier et al. "Inositol hexakisphosphate receptor identified as the clathrin assembly protein AP-2". In: *Biochemical and biophysical research communications* 187.1 (1992), pp. 158–163.

[111] Mitsunori Fukuda et al. "Inositol-1, 3, 4, 5-tetrakisphosphate binding to C2B domain of IP4BP/synaptotagmin II." In: *Journal of Biological Chemistry* 269.46 (1994), pp. 29206–29211.

[112] Stephen K Fisher, James E Novak, and Bernard W Agranoff. "Inositol and higher inositol phosphates in neural tissues: homeostasis, metabolism and functional significance". In: *Journal of neurochemistry* 82.4 (2002), pp. 736–754.

[113] Rui V Simões et al. "Brain metabolite differences in one-year-old infants born small at term and association with neurodevelopmental outcome". In: *American journal of obstetrics and gynecology* 213.2 (2015), 210–e1.

[114] J Larner et al. "Insulin mediators: structure and formation". In: *Cold Spring Harbor symposia on quantitative biology*. Vol. 53. Cold Spring Harbor Laboratory Press. 1988, pp. 965–971.

[115] Farah SL Thong, Chandrasagar B Dugani, and Amira Klip. "Turning signals on and off: GLUT4 traffic in the insulin-signaling highway". In: *Physiology* 20.4 (2005), pp. 271–284.

[116] Farah SL Thong, Philip J Bilan, and Amira Klip. "The Rab GTPase-activating protein AS160 integrates Akt, protein kinase C, and AMP-activated protein kinase signals regulating GLUT4 traffic". In: *Diabetes* 56.2 (2007), pp. 414–423.

[117] Michael J Berridge. "Inositol trisphosphate and calcium signalling mechanisms". In: *Biochimica et Biophysica Acta (BBA)-Molecular Cell Research* 1793.6 (2009), pp. 933–940.

[118] Rosario D'ANNA et al. "Myo-Inositol for the Prevention of Gestational Diabetes Mellitus. A Brief Review". In: *Journal of Nutritional Science and Vitaminology* 65.Supplement (2019), S59–S61.

[119] JF Plows et al. "The Effects of Myo-inositol and Probiotic Supplementation in a High Fat Fed Preclinical Model of Glucose Intolerance in Pregnancy". In: *British Journal of Nutrition* (2019), pp. 1–39.

[120] Hang Lu et al. “Effect of phytase on intestinal phytate breakdown, plasma inositol concentrations, and glucose transporter type 4 abundance in muscle membranes of weanling pigs”. In: *Journal of animal science* 97.9 (2019), pp. 3907–3919.

[121] Hong Xin Wang et al. “Sialylated milk oligosaccharides alter neurotransmitters and brain metabolites in piglets: an In vivo magnetic resonance spectroscopic (MRS) study”. In: *Nutritional neuroscience* (2019), pp. 1–11.

[122] Rebecca J Lepping et al. “Long-chain polyunsaturated fatty acid supplementation in the first year of life affects brain function, structure, and metabolism at age nine years”. In: *Developmental psychobiology* 61.1 (2019), pp. 5–16.

[123] Abed N Azab et al. “Glycogen synthase kinase-3 is required for optimal de novo synthesis of inositol”. In: *Molecular microbiology* 63.4 (2007), pp. 1248–1258.

[124] Helen Maghsudi et al. “Age-related Brain Metabolic Changes up to Seventh Decade in Healthy Humans: Whole-brain Magnetic Resonance Spectroscopic Imaging Study.” In: *Clinical neuroradiology* (2019).

[125] Oron Levin et al. “Sensorimotor cortex neurometabolite levels as correlate of motor performance in normal aging: evidence from a 1H-MRS study”. In: *NeuroImage* (2019), p. 116050.

[126] Marquis P Vawter et al. “Association of Myoinositol Transporters with Schizophrenia and Bipolar Disorder: Evidence from Human and Animal Studies”. In: *Molecular neuropsychiatry* 5.4 (2019), pp. 200–211.

[127] Yukihiko Shirayama et al. “Myo-inositol, glutamate, and glutamine in the prefrontal cortex, hippocampus, and amygdala in major depression”. In: *Biological Psychiatry: Cognitive Neuroscience and Neuroimaging* 2.2 (2017), pp. 196–204.

[128] Amiram I Barkai et al. “Reduced myo-inositol levels in cerebrospinal fluid from patients with affective disorder.” In: *Biological psychiatry* (1978).

[129] J Levine et al. “Double blind study of inositol versus placebo in depression”. In: *Am J Psychiatry* 152 (1995), pp. 792–794.

[130] Carlee Cleeland et al. “Neurochemical changes in the aging brain: A systematic review”. In: *Neuroscience & Biobehavioral Reviews* (2019).

[131] Yoon Hwan Kim et al. “Metabolomic Analysis Identifies Alterations of Amino Acid Metabolome Signatures in the Postmortem Brain of Alzheimer’s Disease”. In: *Experimental neurobiology* 28.3 (2019), pp. 376–389.

[132] Shaltiel Galit et al. “Effect of valproate derivatives on human brain myo-inositol-1-phosphate (MIP) synthase activity and amphetamine-induced rearing”. In: *Pharmacological Reports* 59.4 (2007), p. 402.

[133] Hady Shimon et al. “Reduced frontal cortex inositol levels in postmortem brain of suicide victims and patients with bipolar disorder”. In: *American Journal of Psychiatry* 154.8 (1997), pp. 1148–1150.

[134] Jing Song et al. “Metabolomic signatures and microbial community profiling of depressive rat model induced by adrenocorticotrophic hormone”. In: *Journal of translational medicine* 17.1 (2019), p. 224.

[135] Chi-Hyeon Yoo et al. “Investigating the metabolic alterations in a depressive-like rat model of chronic forced swim stress: An in vivo proton magnetic resonance spectroscopy study at 7T”. In: *Neurochemistry international* 116 (2018), pp. 22–29.

[136] Haifeng Zhang et al. “The efficacy of myo-inositol supplementation to prevent gestational diabetes onset: a meta-analysis of randomized controlled trials”. In: *The Journal of Maternal-Fetal & Neonatal Medicine* 32.13 (2019), pp. 2249–2255.

[137] Xianshan Guo et al. “Myo-inositol lowers the risk of developing gestational diabetic mellitus in pregnancies: a systematic review and meta-analysis of randomized controlled trials with trial sequential analysis”. In: *Journal of Diabetes and its Complications* 32.3 (2018), pp. 342–348.

[138] Rosario D’Anna et al. “myo-Inositol supplementation and onset of gestational diabetes mellitus in pregnant women with a family history of type 2 diabetes: a prospective, randomized, placebo-controlled study”. In: *Diabetes care* 36.4 (2013), pp. 854–857.

[139] A Santamaria et al. “Clinical and metabolic outcomes in pregnant women at risk for gestational diabetes mellitus supplemented with myo-inositol: a secondary analysis from 3 RCTs”. In: *American journal of obstetrics and gynecology* 219.3 (2018), 300–e1.

[140] Alexandra Howlett, Arne Ohlsson, and Nishad Plakkal. “Inositol in preterm infants at risk for or having respiratory distress syndrome”. In: *Cochrane Database of Systematic Reviews* 7 (2019).

[141] Vittorio Porciatti, Tommaso Pizzorusso, and Lamberto Maffei. “The visual physiology of the wild type mouse determined with pattern VEPs”. In: *Vision research* 39.18 (1999), pp. 3071–3081.

[142] Si Myung Byun and Robert Jenness. “Estimation of free myo-inositol in milks of various species and its source in milk of rats (Rattus norvegicus)”. In: *Journal of dairy science* 65.4 (1982), pp. 531–536.

[143] Elizabeth A Rath and Shirley W Thenen. “Use of tritiated water for measurement of 24-hour milk intake in suckling lean and genetically obese (ob/ob) mice”. In: *The Journal of nutrition* 109.5 (1979), pp. 840–847.

[144] Giulio Srubek Tomassy et al. “Developmental abnormalities of cortical interneurons precede symptoms onset in a mouse model of Rett syndrome”. In: *Journal of neurochemistry* 131.1 (2014), pp. 115–127.

[145] Christine L Torborg and Marla B Feller. “Unbiased analysis of bulk axonal segregation patterns”. In: *Journal of neuroscience methods* 135.1-2 (2004), pp. 17–26.

[146] Cleopatra Kozlowski and Robby M Weimer. “An automated method to quantify microglia morphology and application to monitor activation state longitudinally in vivo”. In: *PloS one* 7.2 (2012), e31814.

[147] Cristopher M Niell and Michael P Stryker. "Modulation of visual responses by behavioral state in mouse visual cortex". In: *Neuron* 65.4 (2010), pp. 472–479.
[148] Mikhail Y Frenkel et al. "Instructive effect of visual experience in mouse visual cortex". In: *Neuron* 51.3 (2006), pp. 339–349.
[149] Nathaniel B Sawtell et al. "NMDA receptor-dependent ocular dominance plasticity in adult visual cortex". In: *Neuron* 38.6 (2003), pp. 977–985.
[150] Cristopher M Niell and Michael P Stryker. "Highly selective receptive fields in mouse visual cortex". In: *Journal of Neuroscience* 28.30 (2008), pp. 7520–7536.
[151] Rahmat Muhammad. "The mouse visually evoked potential: neural correlates and functional applications". PhD thesis. Massachusetts Institute of Technology, 2008.
[152] Gianna Muir-Robinson, Bryan J Hwang, and Marla B Feller. "Retinogeniculate axons undergo eye-specific segregation in the absence of eye-specific layers". In: *Journal of Neuroscience* 22.13 (2002), pp. 5259–5264.
[153] Rosa C Paolicelli et al. "Synaptic pruning by microglia is necessary for normal brain development". In: *science* 333.6048 (2011), pp. 1456–1458.
[154] Tania A Seabrook et al. "Retinal input regulates the timing of corticogeniculate innervation". In: *Journal of Neuroscience* 33.24 (2013), pp. 10085–10097.
[155] Peter W Land, Elizabeth Kyonka, and L Shamalla-Hannah. "Vesicular glutamate transporters in the lateral geniculate nucleus: expression of VGLUT2 by retinal terminals". In: *Brain research* 996.2 (2004), pp. 251–254.
[156] Sebastian Werneburg et al. "Targeted complement inhibition at synapses prevents microglial synaptic engulfment and synapse loss in demyelinating disease". In: *bioRxiv* (2019), p. 841601.
[157] Helmut Kettenmann et al. "Physiology of microglia". In: *Physiological reviews* 91.2 (2011), pp. 461–553.
[158] Axel Nimmerjahn, Frank Kirchhoff, and Fritjof Helmchen. "Resting microglial cells are highly dynamic surveillants of brain parenchyma in vivo". In: *Science* 308.5726 (2005), pp. 1314–1318.
[159] Parizad M Bilimoria and Beth Stevens. "Microglia function during brain development: new insights from animal models". In: *Brain research* 1617 (2015), pp. 7–17.
[160] Ilia D Vainchtein et al. "Astrocyte-derived interleukin-33 promotes microglial synapse engulfment and neural circuit development". In: *Science* 359.6381 (2018), pp. 1269–1273.
[161] Akiko Miyamoto et al. "Microglia contact induces synapse formation in developing somatosensory cortex". In: *Nature communications* 7 (2016), p. 12540.
[162] Georg W Kreutzberg. "Microglia: a sensor for pathological events in the CNS". In: *Trends in neurosciences* 19.8 (1996), pp. 312–318.

[163] Elisa R Zanier et al. “Shape descriptors of the “never resting” microglia in three different acute brain injury models in mice”. In: *Intensive care medicine experimental* 3.1 (2015), p. 7.

[164] Keiko Ohsawa et al. “Microglia/macrophage-specific protein Iba1 binds to fimbrin and enhances its actin-bundling activity”. In: *Journal of neurochemistry* 88.4 (2004), pp. 844–856.

[165] Sonia George et al. “Microglia affect α-synuclein cell-to-cell transfer in a mouse model of Parkinson’s disease”. In: *Molecular neurodegeneration* 14.1 (2019), pp. 1–22.

[166] Christian Madry et al. “Microglial ramification, surveillance, and interleukin-1β release are regulated by the two-pore domain K+ channel THIK-1”. In: *Neuron* 97.2 (2018), pp. 299–312.

[167] Iris Bertha Hovens, Csaba Nyakas, Regien Geertruida Schoemaker, et al. “A novel method for evaluating microglial activation using ionized calcium-binding adaptor protein-1 staining: cell body to cell size ratio”. In: *Neuroimmunol Neuroinflammation* 1 (2014), pp. 82–8.

[168] Matthew C Judson et al. “Evidence of cell-nonautonomous changes in dendrite and dendritic spine morphology in the met-signaling–deficient mouse forebrain”. In: *Journal of Comparative Neurology* 518.21 (2010), pp. 4463–4478.

[169] Robert T Fremeau Jr et al. “The expression of vesicular glutamate transporters defines two classes of excitatory synapse”. In: *Neuron* 31.2 (2001), pp. 247–260.

[170] Bo Xiao et al. “Homer regulates the association of group 1 metabotropic glutamate receptors with multivalent complexes of homer-related, synaptic proteins”. In: *Neuron* 21.4 (1998), pp. 707–716.

[171] Sandeep K Singh et al. “Astrocytes assemble thalamocortical synapses by bridging NRX1α and NL1 via Hevin”. In: *Cell* 164.1 (2016), pp. 183–196.

[172] Minzi Chang, Nobuko Suzuki, and Hideki Derek Kawai. “Laminar specific gene expression reveals differences in postnatal laminar maturation in mouse auditory, visual, and somatosensory cortex”. In: *Journal of Comparative Neurology* 526.14 (2018), pp. 2257–2284.

[173] Jason E Coleman et al. “Rapid structural remodeling of thalamocortical synapses parallels experience-dependent functional plasticity in mouse primary visual cortex”. In: *Journal of Neuroscience* 30.29 (2010), pp. 9670–9682.

[174] Hiroyuki Hioki. “Compartmental organization of synaptic inputs to parvalbumin-expressing GABAergic neurons in mouse primary somatosensory cortex”. In: *Anatomical science international* 90.1 (2015), pp. 7–21.

[175] Anderson M Winkler et al. “Multi-level block permutation”. In: *Neuroimage* 123 (2015), pp. 253–268.

[176] US Food, Drug Administration, et al. *CFR-code of federal regulations title 21 section 107.100*. 2019.

[177] Harvey E Indyk and David C Woollard. "Determination of free myo-inositol in milk and infant formula by high-performance liquid chromatography". In: *Analyst* 119.3 (1994), pp. 397–402.

[178] Francesco Corrado and Angelo Santamaria. "Myoinositol Supplementation on Insulin Resistance in Gestational Diabetes". In: *Glucose Intake and Utilization in Pre-Diabetes and Diabetes*. Elsevier, 2015, pp. 229–234.

[179] Tetsuo Ohnishi et al. "Defective craniofacial development and brain function in a mouse model for depletion of intracellular inositol synthesis". In: *Journal of Biological Chemistry* 289.15 (2014), pp. 10785–10796.

[180] Shuang-An Li et al. "Dietary myo-inositol deficiency decreased intestinal immune function related to NF-κB and TOR signaling in the intestine of young grass carp (Ctenopharyngodon idella)". In: *Fish & shellfish immunology* 76 (2018), pp. 333–346.

[181] Romina Marone et al. "Targeting phosphoinositide 3-kinase—moving towards therapy". In: *Biochimica et Biophysica Acta (BBA)-Proteins and Proteomics* 1784.1 (2008), pp. 159–185.

[182] Alan R Saltiel and C Ronald Kahn. "Insulin signalling and the regulation of glucose and lipid metabolism". In: *Nature* 414.6865 (2001), p. 799.

[183] Jeffrey A Engelman. "Targeting PI3K signalling in cancer: opportunities, challenges and limitations". In: *Nature Reviews Cancer* 9.8 (2009), p. 550.

[184] Cuilin Zhang et al. "Maternal plasma 25-hydroxyvitamin D concentrations and the risk for gestational diabetes mellitus". In: *PloS one* 3.11 (2008), e3753.

[185] Mark P Thomas and Barry VL Potter. "The enzymes of human diphosphoinositol polyphosphate metabolism". In: *The FEBS journal* 281.1 (2014), pp. 14–33.

[186] Yasutomi Nishizuka. "Studies and perspectives of protein kinase C". In: *Science* 233.4761 (1986), pp. 305–312.

[187] RF Irvine. "'Quanta'Ca2+ release and the control of Ca2+ entry by inositol phosphates-a possible mechanism". In: *FEBS letters* 263.1 (1990), pp. 5–9.

[188] Michael J Berridge. "The inositol trisphosphate/calcium signaling pathway in health and disease". In: *Physiological reviews* 96.4 (2016), pp. 1261–1296.

[189] Claire EJ Cheetham et al. "Pansynaptic enlargement at adult cortical connections strengthened by experience". In: *Cerebral cortex* 24.2 (2012), pp. 521–531.

[190] Tsvetan Serchov et al. "Increased signaling via adenosine A1 receptors, sleep deprivation, imipramine, and ketamine inhibit depressive-like behavior via induction of Homer1a". In: *Neuron* 87.3 (2015), pp. 549–562.

[191] Dhani Raj Chhetri. "Myo-Inositol and Its Derivatives: Their Emerging Role in the Treatment of Human Diseases". In: *Frontiers in pharmacology* 10 (2019), p. 1172.

[192] Galit Shaltiel et al. "Valproate decreases inositol biosynthesis". In: *Biological psychiatry* 56.11 (2004), pp. 868–874.

[193] Limin Mao et al. “The scaffold protein Homer1b/c links metabotropic glutamate receptor 5 to extracellular signal-regulated protein kinase cascades in neurons”. In: *Journal of Neuroscience* 25.10 (2005), pp. 2741–2752.

[194] Miao-Miao Lv et al. “Down-regulation of Homer1b/c attenuates group I metabotropic glutamate receptors dependent Ca2+ signaling through regulating endoplasmic reticulum Ca2+ release in PC12 cells”. In: *Biochemical and biophysical research communications* 450.4 (2014), pp. 1568–1574.

[195] Andrea de Bartolomeis et al. “Chronic treatment with lithium or valproate modulates the expression of Homer1b/c and its related genes Shank and Inositol 1, 4, 5-trisphosphate receptor”. In: *European Neuropsychopharmacology* 22.7 (2012), pp. 527–535.

[196] Wayne W Tschetter et al. “Refinement of spatial receptive fields in the developing mouse lateral geniculate nucleus is coordinated with excitatory and inhibitory remodeling”. In: *Journal of Neuroscience* 38.19 (2018), pp. 4531–4542.

[197] Guy C Brown and Jonas J Neher. “Microglial phagocytosis of live neurons”. In: *Nature Reviews Neuroscience* 15.4 (2014), p. 209.

[198] Maureen Cowan and William A Petri Jr. “Microglia: immune regulators of neurodevelopment”. In: *Frontiers in immunology* 9 (2018), p. 2576.